Mineralogical Controls on the Ti Isotope Composition of Subduction Zone Magmas

S. Kommescher[1,2,3] , F. Kurzweil[4], R. O. C. Fonseca[2], L. J. A. Rzehak[2] , S. V. Hohl[5] , M. Kirchenbaur[2,4], S. Schuth[2], P. Sprung[6] , and C. Münker[1]

[1]Institut für Geologie und Mineralogie, Universität zu Köln, Köln, Germany, [2]Institut für Geologie, Mineralogie und Geophysik, Ruhr-Universität Bochum, Bochum, Germany, [3]Now at Institut für Mineralogie, Leibniz Universität Hannover, Hannover, Germany, [4]Institut für Mineralogie, Leibniz Universität Hannover, Hannover, Germany, [5]State Key Laboratory of Marine Geology, School of Ocean and Earth Science, Tongji University, Shanghai, China, [6]Hot Laboratory Division (AHL), Paul Scherer Institut, Villigen, Switzerland

Abstract The positive Ti isotope versus SiO_2-content correlation in igneous rocks reflects the fractional crystallization of Ti-bearing oxide minerals. However, Ti isotope variations of subduction-related igneous rocks indicate that the Ti isotope compositions of their mantle sources are heterogeneous and additional mineral phases may promote Ti isotope fractionation. We have determined the Ti isotope composition of well-characterized subduction-related basalts, andesites and boninites. Samples from the Solomon Islands, the Troodos ophiolite in Cyprus, and Cape Vogel in Papua New Guinea show small but resolvable variations that may be related to differences in their mantle sources. Specifically, the $\delta^{49}Ti$ of boninites (+0.109‰ to +0.168‰) is slightly higher than that of tholeiites (−0.027‰ to +0.111‰) from the same localities (Troodos in Cyprus and Cape Vogel in Papua New Guinea). Modeling suggests the partial melting of progressively depleted mantle sources where residual Cr-spinel plays a greater role in controlling the Ti budget during partial melting. More pronounced variations in $\delta^{49}Ti$ are clearly linked to the fractional crystallization of Ti-oxides: Samples from Rabaul Volcanic Complex (New Britain, Papua New Guinea) show increasing $\delta^{49}Ti$ (up to +0.373‰) with increasing Ti/V and decreasing Dy/Yb. Fractional crystallization models suggest that oxide minerals and amphibole are needed to sufficiently increase the $\delta^{49}Ti$ of these magmas. Our study highlights that the combination of diagnostic trace element patterns and Ti isotope compositions in subduction-related igneous rocks can be a powerful tool to constrain petrogenetic processes and to discriminate between different crystallizing mineral phases.

Plain Language Summary Titanium isotope data obtained for basalts from various volcanic arc-related settings show how the different minerals involved in their magmatic evolution influence their Titanium isotope composition. Coupled with trace element concentration data, magmatic processes are revealed that operate on either a large scale, such as along the arc in the 10 km range, or as very specific magma chamber processes.

1. Introduction

Titanium is a refractory, lithophile and mostly fluid-immobile trace element (Kessel et al., 2005) found most abundantly in Earth's oceanic crust. In terrestrial samples, Ti is predominantly tetravalent and primarily hosted in oxide minerals such as rutile, ilmenite and the magnetite-ulvöspinel solid solution, although it can also be enriched in major rock-forming minerals like clinopyroxene, biotite and amphibole. Apart from clinopyroxene, amphibole and (Fe-)Ti-oxides control the Ti budget during the production and differentiation of Island Arc Basalts (IAB; McDonough et al., 1992; Xiong et al., 2005), either by being present as residual minerals during partial melting or as later crystallization products during IAB differentiation (Marxer et al., 2022; Nandedkar et al., 2014; Ulmer et al., 2018). The observed dichotomy of Ti isotope compositions and SiO_2 content in subduction-related rock suites and Ocean Island Basalts (OIB) is thus the result of a complex function of Ti coordination chemistry, redox state (influencing other mineral stabilities), melt structure, water content, and crystallizing mineral modes (Aarons et al., 2021; Deng et al., 2019; Hoare et al., 2020, 2022; Prytulak & Elliott, 2007): The typical coordination of Ti in silicate melts is on average V-fold (Farges, Brown, & Rehr, 1996; Farges et al., 1996a, 1996b; Leitzke et al., 2016). Fractional crystallization of most silicate phases such as olivine, ortho- and clinopyroxene, as well as garnet, is thought to only marginally affect the Ti isotope composition of differentiating silicate melts (Johnson

Resources: S. V. Hohl, M. Kirchenbaur, S. Schuth, C. Münker
Supervision: R. O. C. Fonseca, P. Sprung, C. Münker
Visualization: S. Kommescher, L. J. A. Rzehak
Writing – original draft: S. Kommescher
Writing – review & editing: S. Kommescher, F. Kurzweil, R. O. C. Fonseca, L. J. A. Rzehak, S. V. Hohl, M. Kirchenbaur, S. Schuth, P. Sprung, C. Münker

et al., 2019; Millet et al., 2016; Storck et al., 2023; Wang et al., 2020). Recent studies, however, observed preferential incorporation of lighter Ti isotopes in silicates such as titanite and amphibole (He et al., 2020; Mandl, 2019; Storck et al., 2023). Additionally, Mandl (2019) found that biotite mineral separates to are isotopically lighter than their bulk rock they were separated from, whereas Nie et al. (2021) described biotites that were isotopically heavier compared to the bulk rock. The role of phases like amphiboles and biotite in affecting the Ti isotope composition of the bulk is thus ambiguous, and further work is required (Greber et al., 2021). In contrast, Ti oxides incorporate Ti^{4+} in their VI-fold coordinated site (Alderman et al., 2014; Millet et al., 2016; Mysen & Richet, 2019) and due to the shorter associated Ti-O bond lengths, preferentially incorporate lighter Ti isotopes (Hoare et al., 2022; Millet et al., 2016; Rzehak et al., 2021, 2022; Schauble, 2004). Titano-magnetite (ülvospinel-rich magnetite) displays the largest effect on Ti isotope compositions, followed by ilmenite and then rutile (Hoare et al., 2020, 2022). The degree of fractionation of the individual oxide mineral species is a function of temperature for rutile and ilmenite, whereas the degree of fractionation of magnetite and titano-magnetite are also dependent on its TiO_2 and ülvospinel content, respectively (Hoare et al., 2020, 2022). Consistently, Fe-Ti oxide minerals recovered out of lavas from the Kilauea Iki lava lake are noticeably lighter in their Ti isotope compositions than coexisting silicate phases and glass, which is in good agreement with result from other localities (Greber et al., 2021; Johnson et al., 2019; Mandl, 2019; Storck et al., 2023) and experimental studies (Rzehak et al., 2021, 2022). The involvement of for example, Fe-Ti oxides and amphiboles in the petrogenesis of IAB is therefore expected to result in covariations between their Ti isotope composition and trace element ratios that are diagnostic of the involvement of minerals (e.g., Dy/Yb for amphiboles, Nb/Ta for rutile, or Ti/V for magnetite; David et al., 2000; Davidson et al., 2007; Münker et al., 2004; Shervais, 1982). These possible covariations are a function of what (petrogenetic) process or subduction zone component is most prominent, for example, partial melting of the mantle wedge (a), where the Ti budget is controlled by clinopyroxene and spinel (McDonough et al., 1992), the involvement of slab-derived melts in the presence of rutile, which are linked to variations in Nb/Ta (b) or lastly, fractional crystallization of Ti-oxides and amphiboles in a magma chamber, modifying Ti/V and Dy/Yb (c).

1. Variations in the Ti isotope composition of mantle peridotites and harzburgites were recorded by Anguelova et al. (2022), who find heavier Ti compositions in peridotitic samples (contaminated by recycled material) and contrastingly very light values in highly refractory peridotites, that were possibly subjected to fluid/melt percolation resulting in kinetic Ti isotope effects. Storck et al. (2023) studied arc-related cumulates with distinctly light Ti isotope compositions, complementary to observed heavier isotope compositions in evolved magmas. Studying the effect of possible mantle heterogeneity or source depletion would thus require primitive samples as well as genetically related samples that originate from a more depleted source.

2. After partial melting of the mantle wedge, the involvement of different subduction zone components in arc magmatism (e.g., subducted oceanic crust, their metasedimentary cover and peridotitic material from the overlying mantle wedge; Hawkesworth et al., 1997) with potentially distinct Ti isotope compositions might also account for Ti isotope variability in arc magmas: Eroded felsic material and subducted (meta)sediments are known to display heavier Ti isotope compositions compared to MORB (Greber et al., 2017; Klaver et al., 2021), particularly because isotopically light minerals such as rutile, ilmenite and titano-magnetite are more resistant to weathering (Meinhold, 2010 and references therein). Indeed, Klaver et al. (2021) observe that hydrodynamic sorting of sediments, specifically an enrichment of finer grained Ti-oxides, leads to heavier Ti isotope compositions in the sediment. Consequently, a fitting suite of samples would include a set of igneous samples wherein other studies found inmixing of for example, a hydrous sediment melt into a primitive melt or trace element contribution from the (eclogitic) slab. To complement the set, a selection of sedimentary samples would help constrain the sediment melt endmember.

3. During fractional crystallization, the magnitude of Ti isotope fractionation of rutile and ilmenite and titano-magnetite is a function of temperature (rutile and ilmenite) and TiO_2-content and temperature for titano-magnetite has been calibrated by Hoare et al. (2022). Results for amphiboles are still conflicting; mineral separates from Mandl (2019) are generally isotopically light, whereas Greber et al. (2021) and Storck et al. (2023) only acknowledge that amphibole has at least a part in influencing the Ti isotope budget without any quantification of that effect. Therefore, to study the effect of fractional crystallization of these minerals on the Ti isotopic composition, the required samples need to originate from a (relatively) closed magmatic system, where fractional crystallization of Ti oxides and amphibole has been observed.

Here we present Ti isotope data for basaltic, andesitic and boninitic samples from various subduction zone related settings (Cape Vogel (Papua New Guinea), Upper Pillow Lavas (Troodos, Cyprus), Solomon Islands, Sunda Arc,

and New Britain (Papua New Guinea)), addressing the individual processes. Magmatic samples are complemented by a set of sedimentary samples to evaluate the effect of sediment subduction on the Ti isotope composition of arc magmas (Mediterranean sediments: Kirchenbaur & Münker, 2015; Sunda arc sediments: Kurzweil et al., 2019). By combining Ti isotope compositions with previously published trace element data (Fonseca et al., 2017; Hohl et al., 2022; Kirchenbaur & Münker, 2015; Kirchenbaur et al., 2022; König et al., 2008, 2010; Kurzweil et al., 2019; Schuth et al., 2009), we identify the petrogenetic processes using trace element and isotope modeling and identify the mantle source features that control the Ti isotope composition of subduction-related magmas. Our results have important implications for the future application of stable Ti isotopes as a geochemical indicator for petrogenetic processes operating in subduction zones.

2. Geological Background and Sample Selection

2.1. Upper Pillow Lavas, Troodos Ophiolite Complex (Cyprus)

The Troodos ophiolite complex (TOC) forms the core of the island of Cyprus, and it is a 90 Ma old supra-subduction zone ophiolite (Osozawa et al., 2012; Pearce et al., 1984), which some argue could have also formed at a ridge-trench-trench or ridge-trench-transform fault triple junction (Cameron et al., 1983; Woelki et al., 2019). Heavily serpentinized sequences of ultramafic rocks are overlain by gabbros and a sheeted dyke complex, as well as evolved tholeiitic arc andesites and rare dacites (lower pillow lavas, LPL). These arc tholeiitic lavas are overlain by a series of more primitive pillow lavas, the so-called upper pillow lava units (UPL). While the LPL shows extensive hydrothermal alteration (e.g., affecting its B stable isotope composition, Yamaoka et al., 2015), UPL samples, comprising tholeiites, picrites and high-Ca boninites, are glassy and only display localized low-temperature alteration in the form of glass devitrification and palagonitization (Bednarz & Schmincke, 1989; Fonseca et al., 2017). Troodos samples in this study include tholeiitic basalts ($n = 9$) and high-Ca boninites ($n = 4$) from the UPL. Both basalts and boninites overlap in their SiO_2 contents (47.7–57.9 wt.%, and 53.3 to 58 wt.% respectively), with the boninites generally displaying higher MgO contents (6.81–9.44 wt.%). The UPL has been interpreted to most likely have been emplaced in a subduction zone setting (Fonseca et al., 2017; König et al., 2008, 2010; Rautenschlein et al., 1985; Regelous et al., 2014; Weissel et al., 1982; Woelki et al., 2018). Samples from the UPL have low Nb/Ta and high Nb/La, arguing for petrogenesis without the involvement of rutile (König et al., 2010). The UPL geochemistry is thought to be strongly influenced by subducted (pelagic) sediment components (e.g., Fonseca et al., 2017; König et al., 2010). Hence, samples from the UPL suite represent a suitable endmember to study the influence of subducted sediments on the Ti isotope composition of subduction-related lavas. To better constrain the potential influence of subducted sediments on the Ti isotope composition of the UPL sample suite, we carried out analyses of the Ti isotope composition of five Mediterranean sediment samples drilled during DSDP Leg 16 and ODP Leg 160 (graded sands, limestones, and clast-rich muds; Kirchenbaur & Münker, 2015; Klaver et al., 2015). These samples have been assumed to be a suitable compositional proxy of sediments subducted beneath the Troodos arc during the late Cretaceous (Kirchenbaur & Münker, 2015).

2.2. Cape Vogel (Papua New Guinea)

The Papuan Ultramafic belt is an ophiolite complex that developed during a continent-island arc collision in the late Paleocene (Walker & McDougall, 1982). The ophiolite sequence represents the early stage of island arc magmatism, which formed close to a subduction zone (Jaques & Chappell, 1980). The samples characterized in this study are low-Ca boninites ($n = 7$) and associated tholeiitic basalts ($n = 4$) from Cape Vogel that were previously analyzed for their major and trace elements, and radiogenic isotopes (König et al., 2010) and stable W isotope compositions (Kurzweil et al., 2019). The boninites and boninitic basalts show a limited range in SiO_2 between 55 and 57 wt.% whereas basalts show slightly lower SiO_2 contents (50–53 wt.%). Variations in the Nb/Ta and Zr/Sm of Cape Vogel boninites indicate that their highly depleted mantle sources were flushed by slab melts that formed in the stability field of garnet-amphibolite (Foley et al., 2002; König et al., 2010). This interpretation is supported by co-variations between εHf and Gd/Yb in the boninites (König et al., 2010). Based on this observation, König et al. (2010) suggested that the boninites' trace element budget is mainly controlled by an overprint from slab-derived melts. Because of this, the Cape Vogel sample suite offers the opportunity to assess the potential influence of slab melts derived from mafic oceanic crust on the Ti isotope composition of subduction zone rocks.

2.3. Solomon Islands

The Solomon island arc is located in a complex tectonic setting. Two NW-SE trending island chains mark the collision zone between the Indian-Australian and Pacific plates. This collision zone is active since the Eocene and has been subjected to a reversal of subduction polarity during the Neogene (Schuth et al., 2009 and references therein). Due to the reversal of subduction polarity, young and hot oceanic crust covered by volcanogenic sediments is being actively subducted (Woodlark basin, ca. 4–5 Ma old; Weissel et al., 1982). Samples from the Solomon Island Arc have been the subject of various studies investigating trace element mobility, as well as the general geochemical behavior of HFSE in subduction zones (König & Schuth, 2011; König et al., 2008; Schuth et al., 2004, 2009), which have shown that the HFSE budget is dominated by subducted mafic crust and its overlying volcanogenic sedimentary cover. Therefore, samples from this locality provide a good endmember for arc tholeiites, where subducted pelagic sediments of continental origin are absent. Samples analyzed in this study (Table 1) range from basaltic to basaltic-andesitic compositions (46.7–52.1 wt.% SiO_2), with sub- to super-chondritic Nb/Ta (15.6–26.6). Samples with high Nb/Ta tend to also have high Sr/Y (48–54), which has been interpreted to indicate the partial melting of a subducted slab containing residual rutile (König & Schuth, 2011; Schuth et al., 2009). Investigation of the Solomon Island sample suite for their Ti isotope compositions allows the opportunity to test for the effects of residual rutile in the subducting slab. Moreover, we can test whether the recycling of volcanogenic sediments during subduction could lead to variability of the Ti isotope composition in subduction-related lavas.

2.4. Sunda Arc and Rear Arc (Indonesia)

The Sunda arc is part of the Indonesian arc system and extends from Krakatoa to the islands of Bali and Lombok. Arc volcanism is the result of the subduction of the Indo-Australian plate beneath the Eurasian plate since the Eo-Oligocene (Hall, 2002; Hamilton, 1979; Katili, 1975; van Bemmelen, 1970). The Sunda arc is subdivided into the provinces of East, Central and West Java and Bali-Lombok. Previous trace element and Sr-Hf-Nd-Pb isotope studies reveal a complex magmatic history that involves distinct mantle source components (Gertisser, 2003; Handley et al., 2007, 2011, 2014; Turner & Foden, 2001). Seven sediment samples from the southeast of Java (Site 261 of Deep Sea Drilling Project 27), comprising fine-grained mudstones, limestones, and Fe-Mn-rich samples (Kurzweil et al., 2019), were also analyzed for their Ti isotope composition to assess the influence of subducted sediments on the Ti isotope composition of the Indonesian lavas. Samples studied here originate from the arc (e.g., Krakatoa) and the rear-arc region (e.g., Muriah volcano) ranging from basaltic to basaltic-andesitic compositions (44.8–56.6 wt.% SiO_2). In a similar fashion to our Solomon Island sample suite, Nb/Ta ranges from 15 to 25, with high Nb/Ta-samples showing a tendency to also display elevated Sr/Y (33–55). A negative co-variation between Zr/Sm and Nb/Ta coupled to their high Nb/Ta (Kirchenbaur et al., 2022; Kurzweil et al., 2019) suggests the involvement of rutile in their petrogenesis, specifically the contribution of a slab melt component within the rutile stability field (pressures >1.5 GPa and temperatures <1,150°C; Green & Pearson, 1986; Stolz et al., 1996; Xiong et al., 2005). This possibility has been recently tested by Kirchenbaur et al. (2022), who concluded that the HFSE systematics in Sunda rear-arc samples can best be explained by the slab melting in the presence of residual rutile. As rutile-melt equilibria are known to influence the Ti isotope composition of magmas (Hoare et al., 2022; Millet et al., 2016), the presence of residual rutile in petrogenetic processes is likely to have affected the Ti isotope composition of samples from this locality. As such, the Sunda rear arc suite is another viable target to study the influence that residual rutile has on the Ti isotope composition of subduction-related magmas.

2.5. Rabaul Volcanic Complex, New Britain (Papua New Guinea)

The Island of New Britain (Northwest of Papua New Guinea) formed during the subduction of the Solomon plate beneath the Bismarck plate, ca. 30 Ma ago (Joshima et al., 1986). Latest caldera forming events are dated with 1400 B.P. (Heming, 1974) while current eruptions are still investigated up until recently (e.g., McKee, 2015). The samples analyzed in this study originate from the Rabaul Volcano's inner ($n = 7$) and outer caldera ($n = 3$), and nearby Watom Island ($n = 1$). The studied sample set comprises a differentiation suite of arc-related rocks of basaltic to andesitic compositions (48.5–62.6 wt.% SiO_2; Hohl et al., 2022). High Sr/Nd and U/Th of arc lavas from New Britain suggest that slab-derived fluids, enriched in Sr and U, dominate the inventory of fluid-mobile trace elements (DePaolo & Johnson, 1979), with recent W stable isotope data suggesting fluid mobilization at shallow levels (Kurzweil et al., 2019). The relatively low Nb/Ta between 15 and 19, when compared to the other

Table 1
Titanium Isotope Composition of Analyzed Samples and Reference Materials

Sample ID	Sample type	Location	$\delta^{49}Ti_{OL\text{-}Ti}$	2 s	n	95% c.i.
Cyprus Basalts						
CY 34	Basalt	Kapilio	0.033	0.032	4	0.025
CY4b	Basalt	Kalavasos	0.033	0.370	1	0.048
CY-A	Basalt	Kapilio	0.045	0.010	4	0.008
CY61	Basalt	Akaki River	0.061	0.253	1	0.033
CY 15	Basalt		0.063	0.024	4	0.019
CY-4b	Basalt	Kalavasos	0.070	0.013	4	0.010
ZY-61	Basalt	Akaki River	0.076	0.019	4	0.015
CY-D	Basalt	Kapilio	0.087	0.011	4	0.009
CY63c	Basalt	Kalavasos	0.087	0.268	1	0.035
CY-1	Basalt	Kalavasos	0.090	0.010	4	0.008
CY62	Basalt	Akaki River	0.099	0.262	1	0.034
CY1	Basalt	Kalavasos	0.102	0.269	1	0.035
CY 45	Basalt	Analiondas	0.102	0.027	4	0.021
CY 12	Basalt	Koronia	0.107	0.018	4	0.014
CY 31	Boninite	Kapilio	0.149	0.035	4	0.028
CY 33	Boninite	Kapilio	0.168	0.032	4	0.027
CY 36	Boninite-like	Arakapas	0.146	0.045	4	0.036
CY 39	Boninite	Arakapas	0.166	0.014	4	0.027
Papua New Guinea—Cape Vogel						
PNG 25	Boninite		0.109	0.045	4	0.036
PNG 12	Boninite		0.112	0.031	4	0.024
PNG 1	Boninite		0.114	0.016	4	0.012
PNG 27	Boninite		0.123	0.030	4	0.024
PNG 8	Boninite		0.133	0.040	4	0.032
PNG 14	Boninite		0.136	0.071	4	0.056
PNG 10	Boninite		0.143	0.045	4	0.036
PNG 59	Basalt		−0.027	0.310	1	0.040
PNG 63	Basalt		0.034	0.231	1	0.030
PNG 62	Basalt		0.035	0.016	3	0.020
PNG 54	Basalt		0.110	0.275	1	0.036
Sunda Arc						
I32Ri3	Basalt	Rindjani (arc)	−0.008	0.010	4	0.008
I3Ga1	Basalt	Galunggung (arc)	0.023	0.024	4	0.019
I4Sm1	Basalt	Semeru (arc)	0.045	0.017	4	0.013
I2Kr2	Basaltic Andesite	Krakatau (arc)	0.105	0.028	4	0.022
I29Ag2	Basaltic Andesite	Agung (arc)	0.125	0.016	4	0.013
I12Mu2	Absarokite	Muriah (rear arc)	0.067	0.017	4	0.013
I 25Pe1	Basaltic Andesite	Ringgit (rear arc)	0.082	0.025	4	0.020
I16Mu6	Absarokite	Muriah (rear arc)	0.276	0.026	4	0.020
Solomon Islands						
S 220 SC	Basaltic Andesite	Santa Cruz	0.034	0.031	4	0.024
S 3	Basalt	Ghizo	0.036	0.060	5	0.037

Table 1
Continued

Sample ID	Sample type	Location	$\delta^{49}Ti_{OL\text{-}Ti}$	2 s	n	95% c.i.
S 153 Mbo	Basalt	Mborokua	0.039	0.031	4	0.024
S 18	Basalt	New Georgia, Central	0.042	0.032	4	0.026
S 187 Van	Basalt	Vanikoro, Manieve	0.045	0.026	4	0.021
S 207 Tin	Basalt	Tinakula	0.051	0.036	4	0.028
S 217 SC	Basaltic Andesite	Santa Cruz	0.070	0.012	4	0.009
S E 15	Basalt	Rendova	0.095	0.029	4	0.023
New Britain						
SHR9	Andesite	Inner caldera	0.215	0.012	5	0.007
SHR13	Trachytic Andesite	Inner caldera	0.241	0.029	5	0.018
SHR24	Basaltic Andesite	Inner caldera	0.264	0.022	5	0.014
SHR31	Basaltic Andesite	Inner caldera	0.269	0.012	5	0.007
SHR5	Trachytic Andesite	Inner caldera	0.275	0.014	5	0.009
SHR32	Dacite, trachytic Andesite	Inner caldera	0.373	0.010	5	0.006
SHR16	Basalt	Outer caldera	−0.022	0.023	4	0.018
SHR14	Basalt	Outer caldera	−0.013	0.007	4	0.005
SHR26	Andesite	Outer caldera	0.132	0.028	5	0.017
SHR22	Andesite	Watom Island	0.079	0.032	4	0.025
Sunda arc sediments						
DSDP 27-261-22-2-344.31m	Sandstone		0.206	0.037	4	0.030
DSDP 27-261-3-3-51.33m	Carbonate		0.227	0.021	4	0.017
DSDP 27-261-9-3-202.95m	Mudstone		0.246	0.067	4	0.054
DSDP 27-261-28-2-448.42m	Carbonate		0.475	0.029	4	0.023
DSDP 27-261-6-1-177.41m	Mudstone		0.547	0.008	4	0.007
DSDP 27-261-5-1-162.48m	Mn-oxid-rich muds		0.610	0.007	4	0.006
DSDP 27-261-2-2-11.92m	Mudstone		0.616	0.122	4	0.097
Mediterranean sediments						
DSDP-13-127-18-1-100/102cm	Limestone		0.008	0.033	4	0.027
DSDP-13-127-2-5-140/141cm	Graded sands; marl oozes		0.160	0.024	4	0.027
DSDP-13-128-6-3-50/52cm	Graded silt/sand		0.224	0.050	4	0.040
ODP-160-970-A-9X-1-32/34cm	Clust-rich mud; debris flow		0.185	0.015	4	0.027
ODP-160-970-A-16X-2-44/46cm	Clust-rich mud; debris flow		0.193	0.013	4	0.027
Reference materials						
OL-Ti	Synthetic reference material		0	0.013	10	0.005
Col-Ti	Synthetic reference material		0.210	0.017	10	0.006
JB-2	Natural reference material		−0.043	0.027	2	0.121
BCR-2	Natural reference material		−0.021	0.099	10	0.035
BHVO-2	Natural reference material		0.032	0.017	7	0.008

Note. $\delta^{49}Ti = \delta(^{49}Ti/^{47}Ti)OL\text{-}Ti$. Additional information (selected main and selected trace element data are provided in the supplements see Table S1 in Supporting Information S1.

sample suites investigated here, argue for petrogenesis without the involvement of rutile. The importance of residual Ti-bearing oxide phases was likely negligible during the petrogenesis of these rocks (Woodhead et al., 1998), as indicated by the absence of depletion in Ti and other HFSE in N-MORB normalized trace element patterns in these samples (Hohl et al., 2022; Woodhead et al., 1998). The abundances of fluid-immobile Ti in igneous rocks

from Rabaul follow typical calc-alkaline fractionation trends likely controlled by the fractional crystallization of clinopyroxene, amphibole and (titano-) magnetite (Hohl et al., 2022; Woodhead et al., 1998). As such, the samples from the Rabaul Volcanic Complex (RVC) comprise a co-genetic differentiation suite and thus allow for the investigation of the effect of fractional crystallization on their Ti isotope composition in a relatively closed magmatic system.

3. Methods

3.1. Sample Digestion and Column Chemistry

All dilutions were prepared with Merck Milli-Q 18.2 MΩ cm water and purified acids (p.a. grade, Merck, 24 M HF, 14 M HNO_3 and 10 M HCl purified in Savillex DST-1000 sub-boiling distils). An adequate amount of sample powder (30 μg of sample Ti) and the Cologne $^{49}Ti/^{47}Ti$ double spike were weighed in Savillex vials. Upon visual inspection, most samples were completely dissolved, with only Cape Vogel samples occasionally showing small amounts of black residue (2–3 grains, <0.25 mm large). Whether or not these refractory phases are Ti-rich was tested after data-reduction by screening the determined sample:spike ratio. As the expected sample:spike ratio was reproduced, we assume complete dissolution of Ti-bearing phases. Titanium was purified using a five step column chemistry modified after Tusch et al. (2019), which is described in detail in Kommescher et al. (2020). After column chemistry, samples were dried and then refluxed in 6 M HNO_3–0.1 M HF and H_2O_2 in a 9:1 mixture to remove remaining organic residues. Once dried, samples were re-dissolved in 0.3 M HNO_3–0.0015 M HF for MC-ICP MS measurement.

3.2. MC-ICP-MS Measurements

Samples were measured in the clean-lab facility at the University of Cologne using a Thermo Scientific™ Neptune Plus™ MC-ICP-MS. Samples were introduced using an Elemental Scientific APEX HF desolvating system (flushed with Ar and N_2). For enhanced signal stability, a cyclonic/Scott hybrid spray chamber was placed between the APEX and the injector. The instrument was fitted with Ni sample and Ni (H) skimmer cones. Lens and gas settings were adjusted daily and resolution power (5%–95% peak definition, $\Delta M/M$; Weyer & Schwieters, 2003) was in the range of ~10,000 in high-resolution mode. At the beginning, middle and end of each sequence, multiple spiked aliquots of the Origins Lab reference material (OL-Ti; Millet et al., 2016; Millet & Dauphas, 2014) and the synthetic in-house reference material Col-Ti were measured to monitor long-term drifts and unresolved polybaric interferences. In addition to chemical reference materials, each sequence contained at least one spiked and chemically processed terrestrial rock reference material, which was measured before and after each sample to evaluate the intermediate precision. All ion beams were measured using 10^{11} Ω amplifiers. Sample solutions contained at least 1 μg/mL of Ti, giving intensities of ca. 0.35, 2.5, 3.5, and 2.5×10^{-11} A for ^{46}Ti, ^{47}Ti, ^{48}Ti, and ^{49}Ti, respectively. The measurement solution used for analyses ("on peak zero") gave background intensities that were a factor of 1,000 lower, ca. 0.5, 1, 2 and 1×10^{-14} A for ^{46}Ti, ^{47}Ti, ^{48}Ti, and ^{49}Ti, respectively. Each analysis consisted of the measurement of 60 cycles with 8.4 s integration time each. Data reduction was performed offline using an iterative method described by Compston and Oversby (1969) and improved by Heuser et al. (2002) and Schönberg et al. (2008). All results are given as the deviation of the $^{49}Ti/^{47}Ti$ of the sample relative to the Origins-Lab OL-Ti reference material in permil (Millet & Dauphas, 2014; Millet et al., 2016): $\delta(^{49}Ti/^{47}Ti)_{OL\text{-}Ti} = [(^{49}Ti/^{47}Ti)_{sample}/(^{49}Ti/^{47}Ti)_{OL\text{-}Ti} - 1] \times 1,000$ (henceforth called $\delta^{49}Ti$).

Duplicate measurements constrain the internal precision of the measurement (95% c.i., $n \geq 4$). Over the course of 10 sessions the synthetic reference materials, Col-Ti and OL-Ti, were measured 217 and 86 times, respectively. The measurement precision as determined for Col-Ti and OL-Ti is better than ±0.020‰ (2 s. d., average of 10 measurement sessions). This corresponds to a 95% confidence interval (c.i., calculated using the t-factor for $n - 1$ degrees of freedom, i.e., analyses, times the standard error) of ±0.006‰ and ±0.004‰, for 10 sequences ($n = 10$), respectively (see Figure S1 in Supporting Information S1). Terrestrial reference materials JB-2 and BHVO-2 accurately reproduced previously published values over multiple sessions with −0.043‰ ± 0.027‰ ($n = 2$; 2 s.d.), and +0.031‰ ± 0.017‰ ($n = 7$; 2 s.d.), respectively. Therefore, we assume an intermediate precision of better than ±0.027‰ for Ti isotope analyses. Error bars of individual samples in all Figures reflect either this intermediate precision or the internal precision of sample measurements (95% c.i.), whichever is larger. Total procedural blanks were always below 20 ng Ti, thus contributing less than 0.1% to the total processed sample Ti and are therefore negligible.
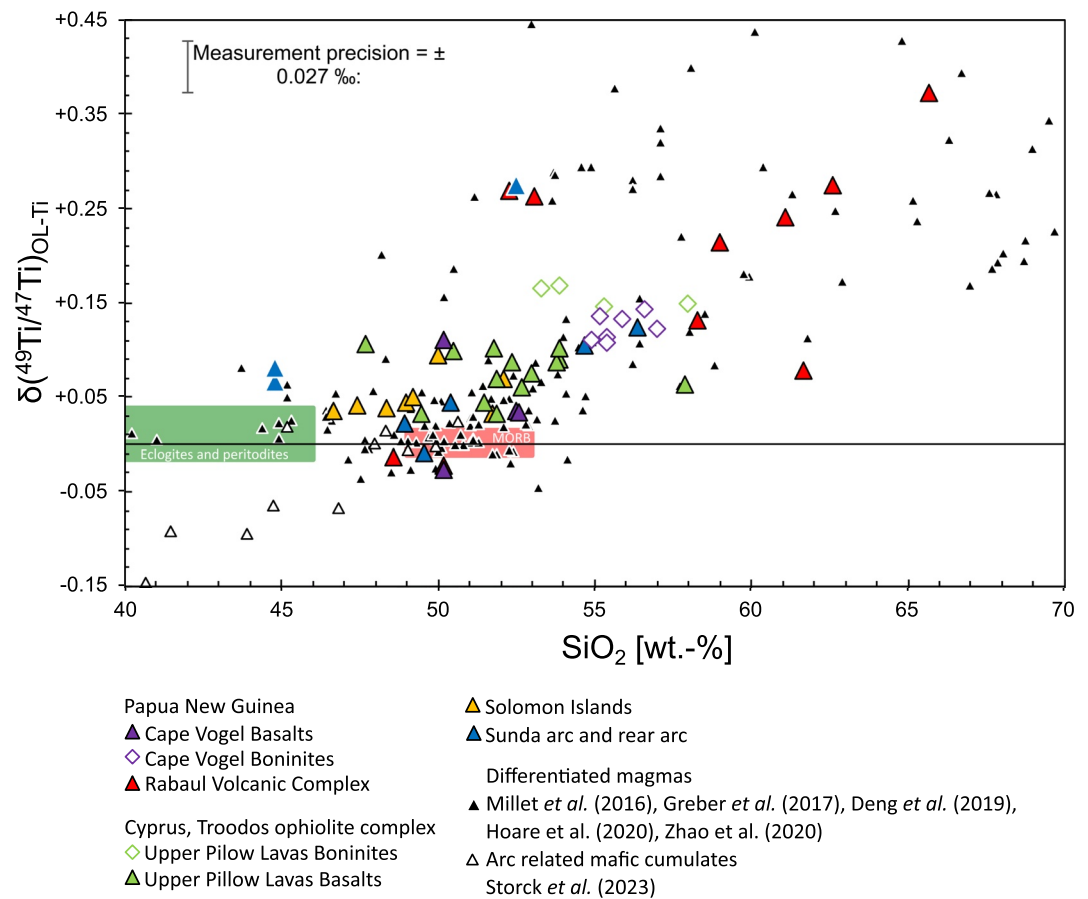
Figure 1. Titanium isotope composition (δ^{49}Ti) of analyzed samples relative to SiO$_2$ (Fonseca et al., 2017; Hohl et al., 2022; Kirchenbaur & Münker, 2015; Kirchenbaur et al., 2022; König et al., 2008, 2010; Kurzweil et al., 2019; Schuth et al., 2009), compared to previous studies (Deng et al., 2019; Greber et al., 2017; Millet et al., 2016; Storck et al., 2023).

4. Results

The Ti stable isotope compositions of each sample suite, including sediment samples and reference materials are listed in Table 1. Tholeiitic basalts from the Troodos UPL suite exhibit δ^{49}Ti between +0.033‰ and +0.102‰, whereas boninites from the same suite show slightly higher values that range between +0.146‰ and + 0.168‰. The drill core sediment samples from the Mediterranean show δ^{49}Ti between +0.008‰ and +0.193‰, which overlap both UPL boninites and tholeiites. Tholeiitic basalts from Cape Vogel have δ^{49}Ti between −0.027‰ and +0.110‰, while associated boninites are again isotopically heavier with δ^{49}Ti between +0.109‰ and +0.143‰. Thus, boninites and boninitic basalts show systematically higher δ^{49}Ti than their associated tholeiites. Basaltic samples from the Solomon Islands arc exhibit only a small variation in δ^{49}Ti between +0.026‰ and +0.095‰. In contrast, basalt, and basaltic andesite samples from the Sunda arc and rear-arc display a broader range of δ^{49}Ti with values between −0.008‰ and +0.276‰. Drill core sediment samples from Site 261 offshore the Sunda arc exhibit Ti isotope compositions that are distinctly heavier and vary between +0.206‰ and +0.616‰. Out of all magmatic samples depicted here, samples from New Britain show the largest variation in δ^{49}Ti, with values between −0.022‰ and +0.373‰. In more detail, three older and less differentiated samples from the outer caldera of the Rabaul Volcano show lower δ^{49}Ti (−0.022‰ to +0.132‰) than samples from the younger and more differentiated inner caldera (+0.215‰ to +0.373‰).

Broadly speaking, the igneous rock samples analyzed in this study show a similar covariation between δ^{49}Ti and SiO$_2$ content as reported in previous studies (Figure 1; Deng et al., 2019; Greber et al., 2017; Hoare et al., 2020; Millet et al., 2016). However, three samples from Rabaul and Sunda show higher δ^{49}Ti than previously found for any other subduction-related samples at a given SiO$_2$ content (ca. 52 wt.%), and rather fall along the "plume-trend" as defined in Deng et al. (2019).

5. Discussion

The chemical composition of subduction zone lavas is intimately linked to the nature of their source components. Such components include variably depleted mantle sources as well as slab-derived melts and fluids. Moreover, subsequent magmatic processes that occur in magma chambers or during magma ascent (e.g., fractional crystallization of minerals or crustal assimilation) are known to modify magma compositions. In this section, we discuss which of these factors play an important role in determining the Ti isotope composition of island arc samples.

5.1. Can δ^{49}Ti Be Used as a Proxy for Hydrous Sediment Melts or Mantle Source Depletion?—Evidence From the Cape Vogel and Troodos Suites

Boninites from the Troodos and Cape Vogel ophiolites have slightly but resolvably higher δ^{49}Ti compared to tholeiites from the same localities (Figure 1). Despite being more SiO_2-rich when compared to arc tholeiites from the same regional setting, boninites derive from relatively undifferentiated primitive magmas, which result from partial melting of a fluid-fluxed depleted mantle wedge. König et al. (2010) showed that the mantle sources of both the Troodos and Cape Vogel boninites are highly depleted, having undergone ca. 10%–20% melt depletion, respectively. As such, the higher δ^{49}Ti of the boninites compared to tholeiites from both sample suites is unlikely to result from fractional crystallization of Fe-Ti oxides, as the lower TiO_2 content of the boninites would imply. Another process is thus required to explain this difference, for example, Fonseca et al. (2017) conclude that the Upper Pillow Lavas reflect melting of a depleted mantle source that was overprinted by hydrous sediment melts.

In the following section, we quantitatively constrain the effect of a sediment melt contribution mixed into a boninitic magma derived from a harzburgitic source (i.e., boninite petrogenesis; Crawford et al., 1989). In a first step, the mixing endmembers need to be defined. The boninitic melt component is formed by partial melting of an ultra-depleted harzburgitic source (Crawford et al., 1989). For this, melting of the Depleted MORB Mantle composition (main elements +0.25% H_2O and mineral modes from Workman & Hart, 2005) was modeled using MELTS (Gualda & Ghiorso, 2015; isobaric sequence, 1,500°C–1,200°C at 1 GPa and ΔFMQ +1) and constrained the main element composition after 30% melt extraction (see Tables S2, S3a, and S5 in Supporting Information S2). The presumptive depleted source consists of 75% olivine, 23% orthopyroxene and 2% spinel and contains 0.013 wt.% TiO_2. The modeled TiO_2 content is consistent with the harzburgite analyzed by Anguelova et al. (2022; 0.014 wt.% TiO_2). The Sr content of this residue was assessed using partition coefficients from Adam and Green (2006; $D_{Sr}^{olivine-melt} = 0.00045$, $D_{Sr}^{ortopyroxene-melt} = 0.0021$, $D_{Sr}^{clinopyroxene-melt} = 0.093$) and Elkins et al. (2008; $D_{Sr}^{spinel-melt} = 0.047$). Using the initial Sr concentration (DMM) of 7.766 μg/g, the model yields 0.015 μg/g Sr in the ultra-depleted residue. Following Fonseca et al. (2017), the hydrous sediment melt end-member was assumed to result from 10% aggregate fractional melting. Bulk-melt partitioning data for sediment melting ($D_{Ti}^{bulk-melt}$ and $D_{Ti}^{bulk-melt}$ of 3.3 and 0.42, Hermann & Rubatto, 2009) indicate that Ti behaves compatibly during partial melting of metasediments, while Sr behaves incompatibly. The Ti and Sr concentrations of the sediment component are constrained by the average TiO_2 content of the analyzed sediments and from Klaver et al. (2015; 0.542 wt.% TiO_2 and 1,590 μg/g Sr). Our models show that Sr and Ti contents of the ultra-depleted source (0.013 wt.% TiO_2 and 0.015 μg/g Sr) are much lower compared to sediment derived melts (0.30 wt.% TiO_2 and 1,759 μg/g Sr), indicating that the in mixing of small volumes of sediment melts into a liquid with a composition similar to the depleted source may drastically change the TiO_2 and Sr content of the final melt.

In a second step, the Sr and Ti concentrations (Equation 1) and isotope compositions (Equation 2a and b) of melt mixtures (90% boninitic melt: 10% sediment melt using Equation 2; Fonseca et al., 2017) were calculated using the following mass balance equations:

$$[c]_M = [c]_{harzburgite} X_{basalt} + \left(1 - X_{harzburgite}\right)[c]_{Sediment} \tag{1}$$

$$
\begin{aligned}
\left(\frac{87_{Sr}}{86_{Sr}}\right)_M &= \left(\frac{87_{Sr}}{86_{Sr}}\right)_{harzburgite} \cdot \left(\frac{[Sr]_{harzburgite} f_{harzburgite}}{[Sr]_M}\right) \\
&+ \left(\frac{87_{Sr}}{86_{Sr}}\right)_{Sediment} \cdot \left(\frac{[Sr]_{Sediment}\left(1 - f_{harzburgite}\right)}{[Sr]_M}\right)
\end{aligned}
\tag{2}
$$

$$\delta^{49}Ti_M = \delta^{49}Ti_{harzburgite} \cdot \left(\frac{[Ti]_{harzburgite} f_{harzburgite}}{[Ti]_M}\right) + \delta^{49}Ti_{MORB} \cdot \left(\frac{[Ti]_{Sediment}\left(1 - f_{harzburgite}\right)}{[Ti]_M}\right) \tag{3}$$

Because no Sr isotope data of our Mediterranean sediment samples were available, we have used the Sr isotope compositions of Mediterranean sediments presented by Klaver et al. (2015) that were also used in Fonseca et al. (2017; i.e., $^{87}Sr/^{86}Sr$ of 0.70895 ± 0.00033). Our sediment samples constrain the $\delta^{49}Ti$ of the sediment melt component ($+0.154‰ \pm 0.170‰$). The Sr isotope composition of harzburgites is taken from Bodinier and Godard (2014 in Figure 21; $^{87}Sr/^{86}Sr$ of 0.7025; 2014). Thus, average sediment melt components are more radiogenic in their Sr isotope composition and heavier in their Ti isotope composition than the boninitic melt source component. Primitive melts derived from the peridotitic mantle are not expected to display significant $\delta^{49}Ti$ variations (see also below): Out of the three harzburgites analyzed by Anguelova et al. (2022), two show $\delta^{49}Ti$ of $-1.523‰$ and $-1.011‰$, likely associated with diffusion-driven isotope fractionation. The third harzburgite (0.014 wt.% TiO_2), displays an $\delta^{49}Ti$ of $-0.002‰$. Given the good agreement of TiO_2 content between MELTS and Anguelova et al. (2022), we use the corresponding $\delta^{49}Ti$ of -0.002 for our source.

Harzburgites contain less Sr but are slightly more radiogenic in their Sr isotope composition compared to the analyzed basalts. Therefore, a much lower sediment melt contribution of <1% is required to model the Sr isotope range of boninitic samples. Assuming that unresolvable Ti isotope fractionation takes place during sediment melting, the $\delta^{49}Ti$ of the hydrous sediment melt would reflect that of the sediments, which is higher than the $\delta^{49}Ti$ of the basalts (Figure 2) but indistinguishable from boninitic values. The analyzed Mediterranean sediments show no relative enrichment in Ti compared to basaltic and boninitic rocks (see Table 1), and the compatible behavior of Ti during sediment melting (Hermann & Rubatto, 2009) would cause even lower Ti contents in the hydrous sediment melt component relative to the metasediments. The in-mixing of a comparatively Ti-rich and isotopically heavy sediment melt into isotopically lighter boninitic melts with lower TiO_2 contents (10% addition of hydrous sediment melt) would increase the $\delta^{49}Ti$ of the melt-mixture up to $+0.114‰$. This is, however, still lower than the boninite average of $+0.150‰$. An unrealistically high sediment melt component of around >80% would be required to explain the observed $\delta^{49}Ti$ and TiO_2 values of boninites. Moreover, such a high proportion of sediment melt component is at odds with the Sr isotope compositions of boninites. It should also be added that the average $\delta^{49}Ti$ of the sediments is slightly above the boninitic value if the one limestone sample close to the zero line is excluded, which only exacerbates the issues of the model. In summary, the inmixing of a hydrous sediment melt into boninitic melts fails to explain the observed $\delta^{49}Ti$ variations in Cyprus boninites.

Given that differences in magmatic differentiation and variable contributions of subduction components cannot explain the higher $\delta^{49}Ti$ in boninitic compared to their tholeiitic counterparts, only one explanation remains— which are differences in source depletion. Tholeiite petrogenesis is dominated by the partial melting of clino- and orthopyroxene, which are the main hosts for Ti in lherzolite (McDonough et al., 1992). This process is expected to cause negligible Ti isotope fractionation as pyroxene/melt equilibria are not known to produce significant Ti isotope fractionation (Wang et al., 2020). This view is supported by the observation that both, Cape Vogel and Upper Pillow Lava tholeiites, which result from pyroxene-controlled partial melting, show a similar range in $\delta^{49}Ti$ (average $\delta^{49}Ti$ of $+0.064‰ \pm 0.078‰$) compared to average mantle peridotites ($+0.012‰ \pm 0.028‰$—see Millet et al., 2016). Boninites, however, are produced through partial melting of an incompatible trace element depleted harzburgitic residual mantle wedge (Hawkins et al., 1984). The harzburgitic sources of low-Ca boninites (Cape Vogel) are even more depleted than the sources of high-Ca boninites (UPL; Crawford et al., 1989). Higher $\delta^{49}Ti$ of the boninites compared to tholeiites could thus be linked to differences in source depletion, and the distribution of Ti between different residual minerals. When compared to tholeiitic mantle sources, the Ti-budget in the highly depleted boninite sources is no longer dominated by clinopyroxene, with residual Cr-spinel playing a greater role (Crawford et al., 1989; McDonough et al., 1992). Spinel is expected to favor light Ti isotopes in the VI-fold coordinated B-site of the spinel structure (e.g., Millet et al., 2016; Okube et al., 2018), so its increased relative modal abundance in boninite mantle sources would be expected to shift the $\delta^{49}Ti$ of any partial melt derived from these sources toward heavier values.

To test whether partial melting of variably depleted mantle sources can indeed explain the observed difference in the $\delta^{49}Ti$ of tholeiitic and boninitic Troodos and Cape Vogel suites, we have carried out several partial melting models using Rhyolite MELTS (Gualda & Ghiorso, 2015). We began by modeling the mineral modal abundances of the residue and the TiO_2 contents of the silicate melt that results from partial melting of a depleted MORB mantle source (DMM; after Workman & Hart, 2005, See Tables S3a–S3c and S4 in Supporting Information S2). The model was carried out at slightly hydrous conditions (2% H_2O), a constant pressure of 1 GPa and between 1,100 and 1,400°C and an fO_2 of FMQ + 1. We additionally constrain the evolution of the Zr and Ti content of the melt using partitioning data by Adam and Green (2006; $D_{Zr}^{olivine-melt} = 0.0015$, $D_{Zr}^{orthopyroxene-melt} = 0.0099$,

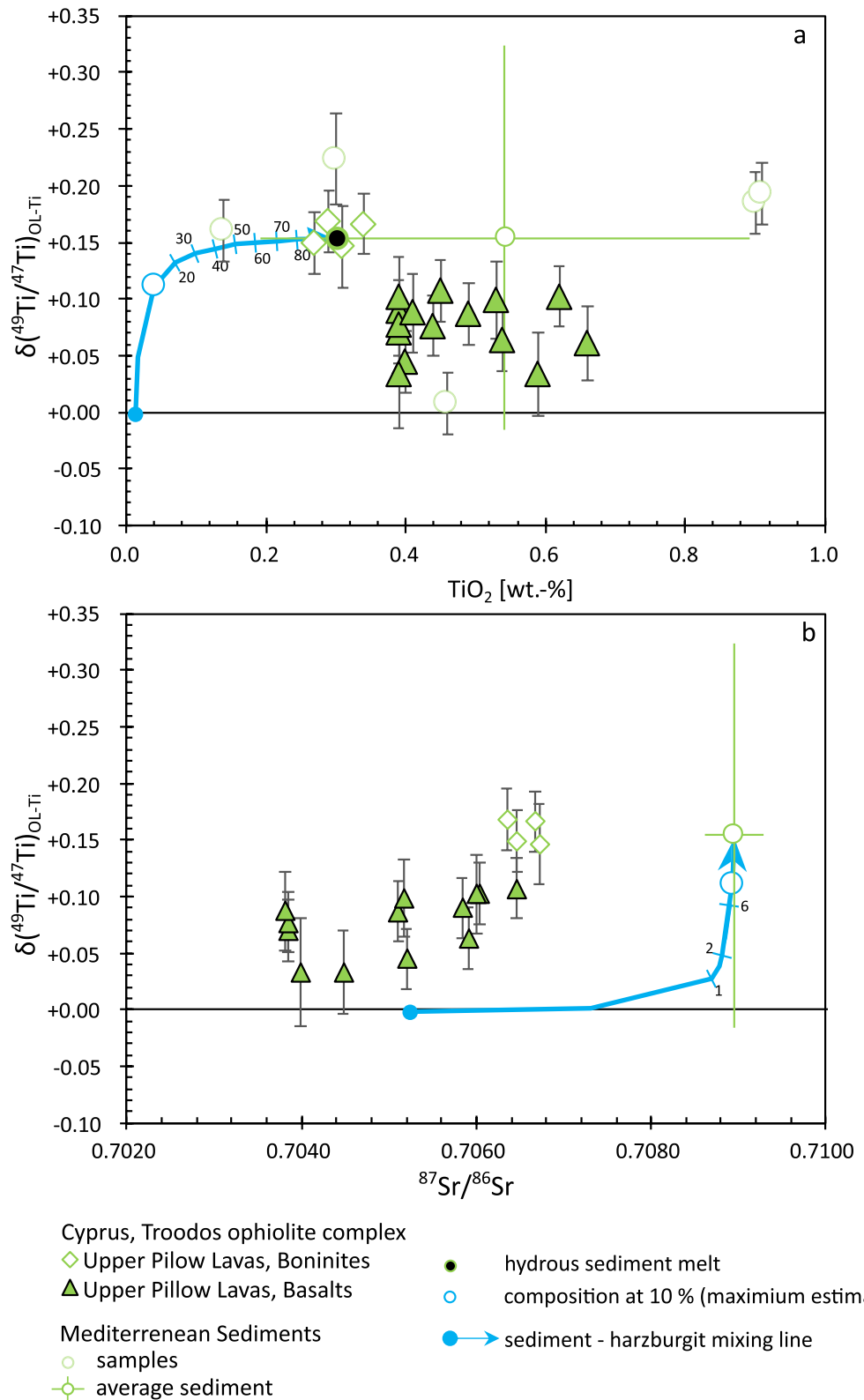**Figure 2.** $\delta^{49}Ti$ versus TiO_2 and $^{87}Sr/^{86}Sr$ for Cyprus UPL. Assuming magma mixing with no resolvable Ti isotope fractionation, the blue circle is the predicted composition when 10% of a hydrous sediment melt is mixed into melt derived from an ultra-depleted source, which explained trace element and isotope variations in Fonseca et al. (2017). Strontium isotope data for Mediterranean sediments are from Klaver et al. (2015), average Sr contents are from MORB by White and Klein (2014) and Ti isotope composition of the harzburgitic source is from Anguelova et al. (2022).

$D_{Zr}^{clinopyroxene-melt} = 0.064$) and Klemme et al. (2006; $D_{Zr}^{spinel-melt} = 0.56$). Model conditions were chosen to reflect the initial stages of subduction-related magmatism, where some minor dehydration of the subducting slab has already taken place in an oxidized mantle wedge. In a second step, we modeled partial melting of the residue after ~5, 10, and 20% melt. The solid phases and major elements are provided by Rhyolite MELTS. The concentration of Zr in the restite after 10% melt extraction is calculated according to Shaw (1970) using

$$[Zr]_{residue} = D_{Zr}^{solid-melt} * [Zr]_{melt} \text{ with } [Zr]_{melt} = [Zr]_0/F \cdot \left(1 - (1-F)^{(1/D)}\right), \tag{4}$$

where $[Zr]_0$ is the initial Zr concentration of DMM (5.082 µg/g after Workman & Hart, 2005), F is the degree of melting (0.1) and D the bulk melt partition coefficient. This results in 1.4 µg/g Zr, corresponding to a Ti/Zr of ~0.4 in the residue. Cameron et al. (1983) argued that a certain amount of water must have been present in the boninitic mantle source to induce melting, so our melting assemblage is refluxed with 1.5 wt.% of water. We use the same conditions, partitioning data, and fractionation factors as before, calculations are again stopped after 25% partial melting. The aim of this first step was to reproduce the expected change in the residue composition during tholeiite petrogenesis from lherzolitic to harzburgitic residue. The Ti isotope composition of both residue and silicate melt was then calculated via a Rayleigh distillation model according to:

$$({}^{49}Ti/{}^{47}Ti)_{melt} = ({}^{49}Ti/{}^{47}Ti)_{initial} \cdot \left(f Ti^{(\alpha_{bulk-melt}-1)}\right) \tag{5}$$

The $\alpha_{bulk-melt}$ for each calculation step is determined according to the $\Delta^{49}Ti_{bulk-melt}$ using the $\Delta^{49}Ti_{opx-melt} = -0.002‰$ and the $\Delta^{49}Ti_{cpx-melt} = -0.035‰$ from Rzehak et al. (2021, 2022). Most recent studies show that $\Delta^{49}Ti_{oxide-melt}$ is a function of for example, TiO_2 content in oxides and temperature (Hoare et al., 2022) or the degree of polymerization of the melt (Aarons et al., 2021). Our MELTS model estimates the TiO_2 content of the spinel to be below 0.5 wt.% TiO_2, consistent with the range of natural peridotite-derived spinels (0.02–1.0 wt.% TiO_2; Witt-Eickschen & O'Neill, 2005). The calibration by Hoare et al. (2022) is thus not ideal in our case, given that the calibration works with oxides containing between 10 and 20 wt.% TiO_2. Because of the uncertainty of ±0.1203 near the intercept and the need to extrapolate well beyond 10 wt.% TiO_2, we hence use the approach by Aarons et al. (2021) and determine $\Delta^{49}Ti_{spinel-melt}$ via the force constants of the Ti-O bonds in the mineral of interest: The force constant $\langle F \rangle_{spinel}$ is related to the $\Delta^{49}Ti_{spinel-melt}$ via

$$\Delta^{49}Ti_{spinel-melt} = 3815 \frac{\langle F \rangle_{spinel} - \langle F \rangle_{melt}}{T^2} \tag{6}$$

The $\langle F \rangle_{melt}$ parameter is calculated via the degree of polymerization of the melt that is, the ratio of non-bridging oxygen per tetrahedrally coordinated atom (NBO/T, Aarons et al., 2021; Mills, 1993) with

$$\langle F \rangle_{melt} = -60 \cdot NBO/T + 463. \tag{7}$$

Finally, the force constant $\langle F \rangle_{spinel}$ is calculated via

$$\langle F \rangle_{spinel} = 3x/\langle F \rangle_1 + (1 - 3x/2)\langle F \rangle_2 \tag{8}$$

with $x = Fe^{3+}/(Fe^{2+} + Fe^{3+})$ in the spinel. Iron contents of the spinels are given by MELTS, the force constants $\langle F \rangle_{1,2}$ correspond to the force constants of Ti-bonds in titano-magnetite (296 N/m) and ulvöspinel (309 N/m; Aarons et al., 2021). This way, both melt depolymerization and the NBO/T can be calculated using the major element data provided by MELTS, $\langle F \rangle_{melt}$ in our models varies between 402 and 422 N/m, $\langle F \rangle_{spinel}$ is typically in the range of 300.3 ± 0.025 N/m.

The new lherzolitic to harzburgitic source compositions after for example, 10% partial melting of DMM consist of 6.4% clinopyroxene, 3.6% spinel, 29.3% orthopyroxene and 60.6% olivine. The depleted source contains 0.066 wt.% TiO_2, with a putative $\delta^{49}Ti_{depleted\ source}$ of $-0.018‰$. The observed trend toward lower TiO_2 and $\delta^{49}Ti$ is consistent with the analyzed harzburgite by Anguelova et al. (2022; 0.014 wt.% TiO_2, $\delta^{49}Ti$ of $-0.002‰$).

During clinopyroxene-mediated melting (first step, green lines in Figures 3a and 3b), the Ti/Zr_{melt} and $TiO_{2,\ melt}$ increase with continuous depletion of the residue. Once clinopyroxene is exhausted (~10% partial melting), the TiO_2 content of the melt steadily decreases as predominantly olivine and orthopyroxene melt in the presence of spinel. Since spinel is present throughout the model, the $\delta^{49}Ti$ of the melt steadily increases slightly as this phase preferentially retains light Ti isotopes in the residue. The evolution line of our model intersects with the basalt array of both tholeiite localities in $\delta^{49}Ti$ versus Ti/Zr and $\delta^{49}Ti$ versus TiO_2 (Figures 3a and 3b). At 25%

Figure 3.
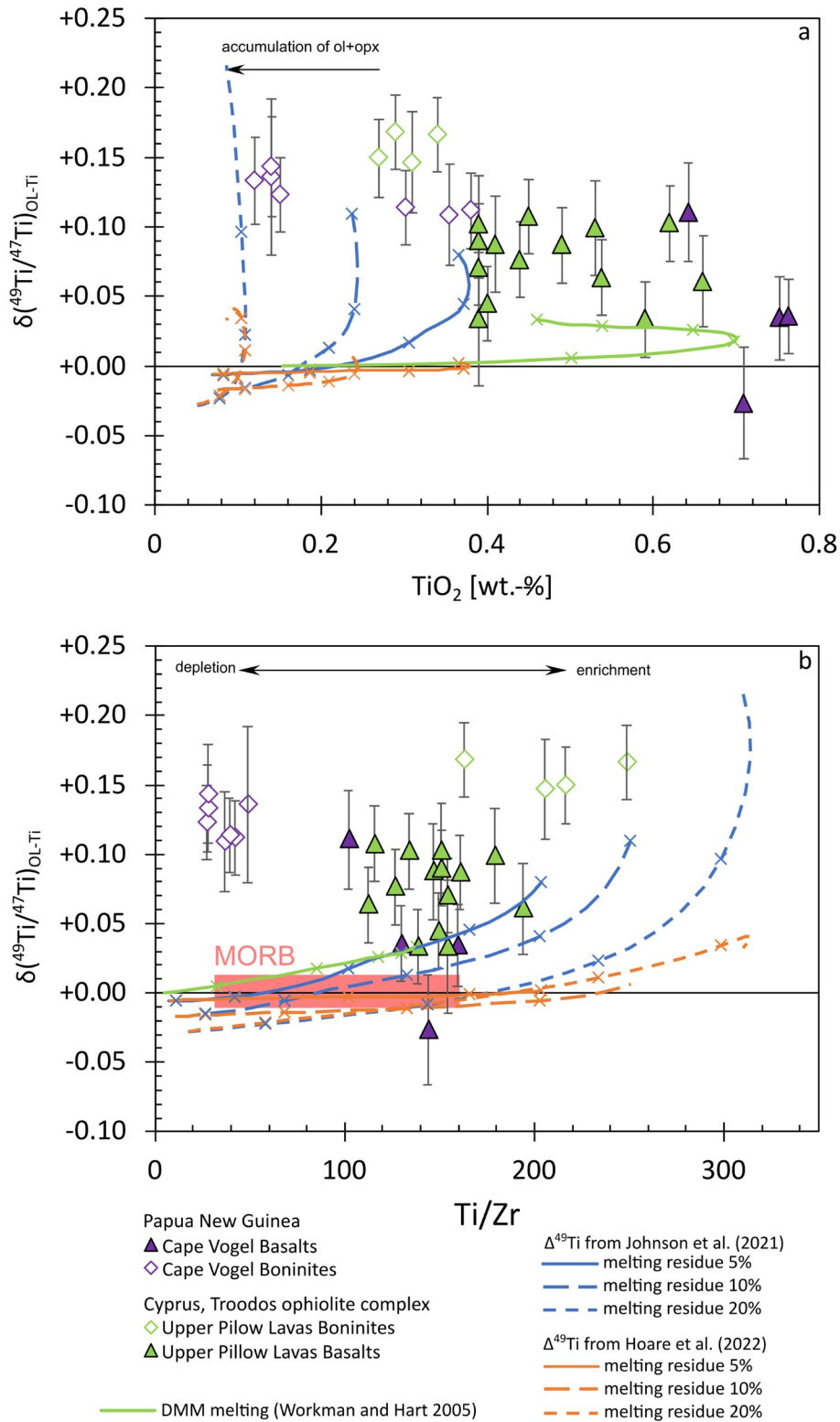
partial melting, the modeled melt contains ~0.46 wt.% TiO_2 at a $\delta^{49}Ti$ of ~+0.03‰ and broadly overlaps with the tholeiitic samples but does not reproduce observed variations in boninites below 0.4 wt.% TiO_2. Therefore, partial melting of the DMM alone cannot explain the observed $\delta^{49}Ti$ in boninites. The TiO_2, Ti/Zr, and $\delta^{49}Ti$ of the more depleted melt steadily increase during clinopyroxene- and predominantly orthopyroxene-controlled melting in the presence of spinel in all models. The 5% source depletion model ends slightly below the region of (UPL) boninitic compositions (Ti/Zr ~ 200, TiO_2 of 0.25 wt.% and $\delta^{49}Ti$ of +0.06‰) after ~25% partial melting (blue lines in Figure 3). The more depleted sources (~10 and 20% depletion) gradually reach higher $\delta^{49}Ti$ and encompass all boninite samples within $\delta^{49}Ti$ and TiO_2 space.

In summary, minor adjustments of source composition allow our initial DMM melting model to accurately describe the Ti isotope compositions and TiO_2 contents of our tholeiites (green lines in Figures 3a and 3b). For boninites, however, partial melting of a spinel-bearing ultra-depleted mantle source is required to explain lower TiO_2 and slightly elevated $\delta^{49}Ti$ above the MORB range (blue lines in Figures 3a and 3b). Minor adjustments of the degree of source depletion (between 5% and 20% depletion Figures 3a and 3b) encompass all boninite samples and accurately reproduce the observed variations. Therefore, the origin of the Ti in tholeiites and boninites from Cyprus and Cape Vogel can be pinpointed to two different positions in the varyingly depleted mantle wedge and varying degrees of partial melting, consistent with literature observations (~25% partial melting of the boninite source, Hawkins et al., 1984; 10% source depletion for Upper Pillow Lavas, ~20% for Cape Vogel; König et al., 2010). This observation is in line with observed small-scale mantle heterogeneity in peridotites, specifically harzburgites (Anguelova et al., 2022).

5.2. The Influence of Subduction Components on the Ti Isotope Composition of Island Arc Lavas—The Solomon Islands and Sunda Suites

Most samples from the Solomon Islands show a similar range in $\delta^{49}Ti$ between +0.034‰ and +0.070‰ (except SE15 with $\delta^{49}Ti$ = +0.095‰), only slightly higher than the average of mantle peridotites (+0.012‰ ± 0.028‰— see Millet et al., 2016), or MORB ($\delta^{49}Ti_{MORB}$ = +0.011‰ ± 0.009‰ (95% c.i.); Deng et al., 2019; Millet et al., 2016). This indicates that the Ti budget of these samples is dominated by processes that produce only negligible Ti isotope fractionation, such as partial melting of peridotite and fractional crystallization of olivine and pyroxene (McDonough et al., 1992). Three samples (one from Solomon Islands, two Sunda rear arc samples) show distinctly superchondritic Nb/Ta, which was associated with partial melting of a subducted slab in the presence of rutile (Kirchenbaur et al., 2022; König & Schuth, 2011; Schuth et al., 2009).

Similar to Section 5.1, drill core sediment samples from Site 261 offshore the Sunda arc exhibit Ti isotope compositions that are distinctly heavier, compared to Sunda arc and rear arc samples ($\delta^{49}Ti$ between +0.2‰ and +0.6‰). However, in contrast to Cyprus sediments, these contain up to 1.6 wt.% TiO_2, a hydrous sediment melt derived from subducted sediments would thus be more enriched in Ti than the melt composition in the Mediterranean sediments. Furthermore, high Th/La ratios, indicating contributions from sediments due to the high incompatibility of Th during partial melting (and fluid immobility), coincide with high $\delta^{49}Ti$ in sediment samples and seemingly correlate with $\delta^{49}Ti$ and Th/La in Sunda arc and rear arc samples. To that effect, a relatively Ti enriched, and isotopically heavy sediment melt derived component may increase the $\delta^{49}Ti$ of a primitive basaltic melt in the Sunda arc. As described above, we modeled the mixing of a primitive basaltic melt (represented by I4Sm1, 1.40 wt.% TiO_2 and $\delta^{49}Ti$ of +0.045 ± 0.027‰) with a sediment derived melt (based on the average composition of the analyzed sediments, 1.33 wt.% and $\delta^{49}Ti$ of +0.418‰). Using the same bulk-melt partitioning data as in 5.1, after 10% partial melting a tentative TiO_2 content of 1.53 wt.% was obtained. Since there is large variation in the sediment samples (0.7–1.8 wt.% TiO_2 and $\delta^{49}Ti$ between +0.206‰ and +0.616‰), we assumed two more initial sediment compositions (low Ti, drill sample 28-2, $\delta^{49}Ti$ of +0.206‰ and high Ti sample 6-5, $\delta^{49}Ti$ of +0.616‰). All mixing models (Figure 4, Table S5 in Supporting Information S2) indicate that excesses of 20% sediment contribution would be required to distinctly increase the $\delta^{49}Ti$ of the modeled mixture. Furthermore, only the low Ti composition evolves toward lower TiO_2 contents, which in turn would require even higher contributions from the sediment melt (>40%) in the Sunda arc lavas. As such, the mixing model fails to explain the observed TI isotope compositions.

Figure 3. Partial melting model of the Depleted MORB Mantle. (a) shows the $\delta^{49}Ti$ versus. Ti/Zr and TiO_2, panel (b) shows the modeled effect of partial melting of the Depleted MORB Mantle (assuming Ti isotope fractionation due to partial melting in the presence of spinel; green trendline; 0.25% water, isobaric at 1 Gpa from 1,100 to 1,400°C at ΔFMQ +1) and melting of the harzburgitic residue after 5%, 10%, and 20% melt extraction (blue, 1 GPa isobaric, 1,100–1,400°C at ΔFMQ +1). Yellow lines show the same models using a $\Delta^{49}Ti_{spinel-melt}$ calculated from Hoare et al. (2022) for comparison. Numbers and tick marks represent melting intervals in percent. Samples PNG 54, 59, and 63 are shown with their 95% c.i, the red box in (a) depicts the MORB range, not shown in (b) due to higher TiO_2 content of MORB that extends the scale of the diagram.
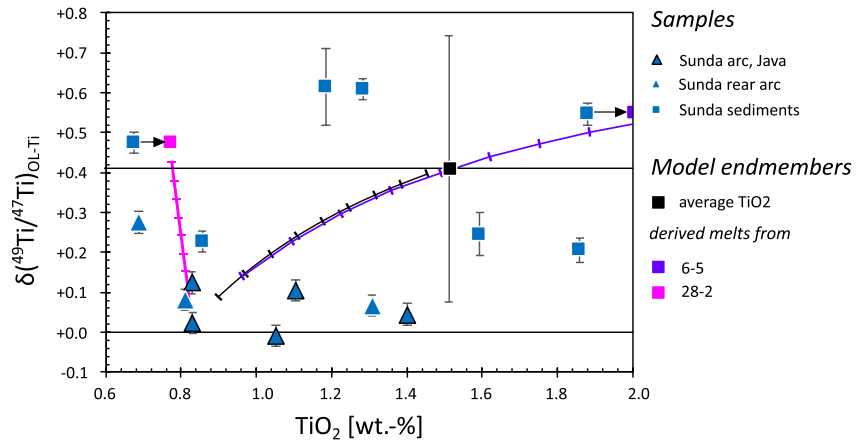
Figure 4. Mixing model between a primitive basalt from the Sunda arc and a hydrous sediment melt compositionally derived from analyzed sediment samples. The increase in δ^{49}Ti versus TiO_2 can only be explained if the initial composition is Ti-poor.

In order to test for the contribution of a slab melt in the stability field of rutile to the Ti isotope budget, we model a rutile bearing slab derived melt. Specifically, we modeled the effect of partial melting in the presence of rutile (Figure 5a) and subsequent fractional crystallization of Ti oxides (see Figures 5a and 5b, details in the figure caption). Following modeling constraints by König and Schuth (2011), we calculated V contents, Nb/Ta and δ^{49}Ti using a non-modal melting model (D_0: 0.425:0.56:0.015 and D_c:0.415:0.56:0.025—cpx:grt:rt) with MORB-like initial concentrations (White & Klein, 2014), partition coefficients from Klemme et al. (2002, garnet; 2005, rutile) and Zhang et al. (2013, clinopyroxene). The bulk-melt fractionation factor was determined using the D_c values above and the Δ^{49}Ti$_{cpx-melt}$ from Rzehak et al. (2021), the Δ^{49}Ti$_{pyrope-melt}$ from Wang et al. (2020) and the Δ^{49}Ti$_{rutile-melt}$ rutile melt from Hoare et al. (Hoare et al., 2022, calculated at 1,050 °C König & Schuth, 2011; Rapp & Watson, 1995), which results in a Δ^{49}Ti$_{bulk-melt}$ of −0.040‰ (see Table S6 in Supporting Information S2). We further include data from the Rabaul samples as a benchmark for the influence fractional crystallization processes onto the Ti isotope budget (see the next section). Fractional crystallization (red trends, Figures 5a and 5b) is calculated using the experimental mineral assemblages of an evolving hydrous arc basalt (Ulmer et al., 2018) and the same parameters as before, with additional V concentrations for global MORB (White & Klein, 2014; see Section 5.3 for details on the mineral-melt partition coefficients). Indeed, the partial melting model would produce a sample with a δ^{49}Ti ~ +0.05‰ at high Nb/Ta, consistent with observed Nb/Ta and δ^{49}Ti in, for example, SE15. However, Sunda arc and rear arc lavas exhibit a negative covariation between δ^{49}Ti with V (Figure 5b).

This negative covariation of V and δ^{49}Ti indicate fractional crystallization of either clinopyroxene (e.g., $D_V^{clinopyroxene-mel}$ ~ 3; Adam & Green, 2006) or Ti-rich oxide minerals such as ilmenite or (titano-)magnetite (e.g., $D_V^{ilmenite-melt}$ ~ 16, Klemme et al., 2006; $D_V^{magnetite-melt}$ ~ 14, Sievwright et al., 2017). The absence of a negative covariation in MgO versus Sc or V versus Sc in Sunda and Solomon Island samples argues against significant fractional crystallization of clinopyroxene (now shown; David et al., 2000). Furthermore, the fractional crystallization of clinopyroxene would barely affect the stable Ti isotope composition of the lava. In contrast, Fe-Ti oxides preferentially incorporate light Ti and fractional crystallization of Fe-Ti oxides was shown to be the predominant process leading to Ti isotope fractionation (Hoare et al., 2020, 2022; Johnson et al., 2019; Millet et al., 2016). Although our Sunda samples comprise multiple differentiation suites with no clear co-genetic relationship, the δ^{49}Ti versus V pattern in the arc samples (Figure 5b) most likely reflects different degrees of fractional crystallization of oxide minerals during magma ascent. While Sunda rear-arc samples and sample SE15 from the Solomon Islands may initially have shown a distinct signature related to slab melt derived from a rutile-bearing residue, at its present stage, the contribution of slab melts is likely overprinted by fractional crystallization of Ti oxides. Specifically, the covariations of δ^{49}Ti and trace elements (e.g., SiO_2, in Figure 1) of the analyzed Sunda (rear) arc samples are broadly consistent with fractional crystallization processes (Figure 5b, red model line). This process would, outside of rutile stability, cause a δ^{49}Ti variation at constant Nb/Ta, irrespective of what oxide species is chosen during crystallization (ilmenite, titano-magnetite, Figure 5a). In conclusion, individual samples may show the influence of a slab melt derived from a rutile-bearing residue on the Ti isotope composition, but the dominance of widespread fractional crystallization processes obscures this effect.
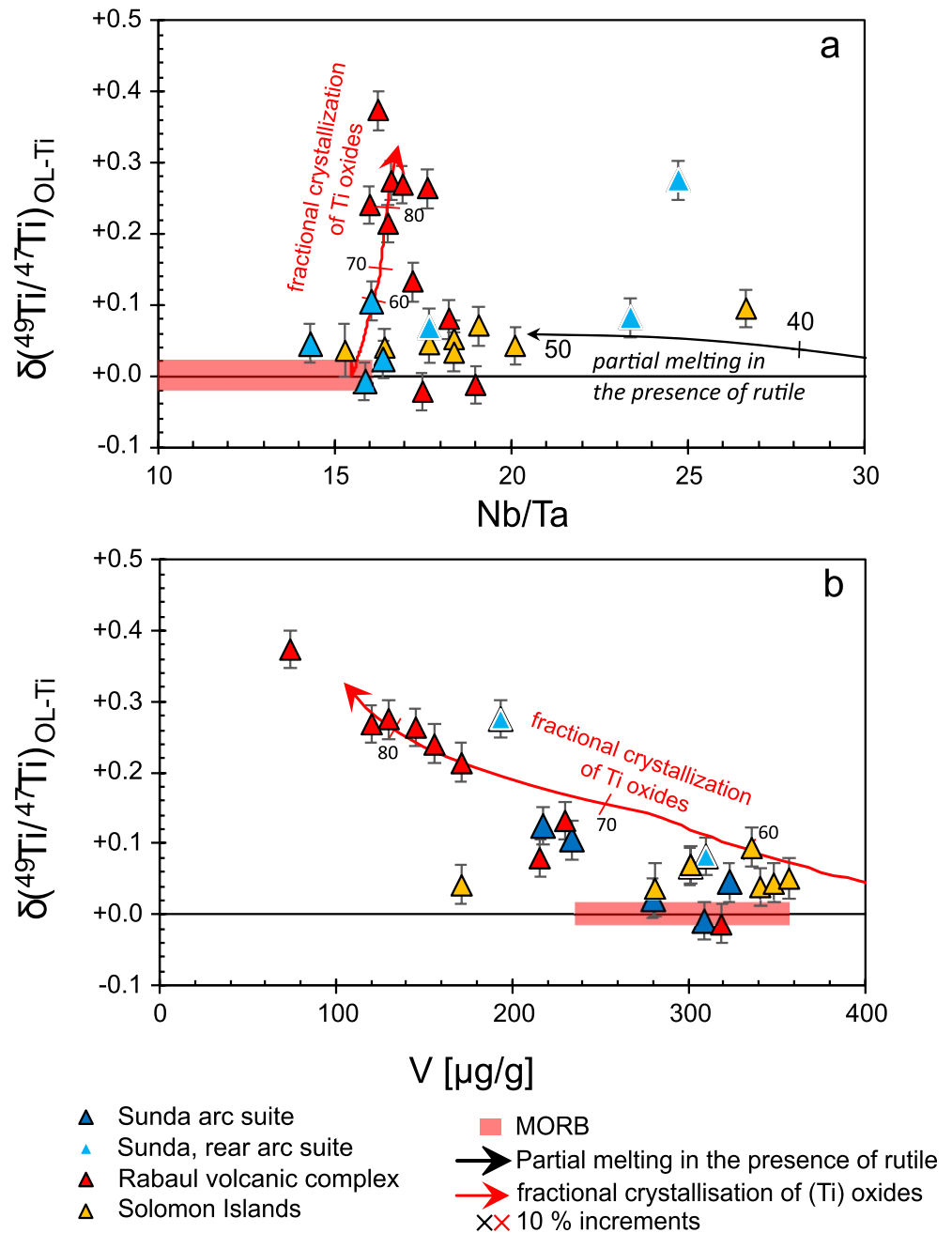
Figure 5. Panel (a) $\delta^{49}Ti$ versus Nb/Ta for the same samples showing the potential effect of partial melting in the presence of rutile, higher Nb/Ta suggest the presence of rutile during partial melting, in the case of Solomon Islands in the slab component. Data from Rabaul is shown for process-comparison, see Section 5.3 for details. Panel (b) $\delta^{49}Ti$ versus V contents of samples from the Sunda arc, Solomon Islands, and Rabaul Volcanic Complex, showing indications for V removal and Ti isotope fractionation through fractional crystallization of Ti-rich oxides—(red arrow; trace element data from Hohl et al., 2022; Kirchenbaur et al., 2022; Schuth et al., 2009).

5.3. The Effects of Polymineralic Fractional Crystallization—Rabaul, New Britain Arc, Papua New Guinea

Samples from the RVC in New Britain comprise a differentiation suite including basaltic to andesitic rocks. The least differentiated samples are from the older outer caldera with an age of ~7,000 before present (B.P.; McKee, 2015). A slightly younger sample from the outer caldera was collected at the flank of the Palanagaia Volcano, yielding an age of ~1400 B.P. (Heming, 1974). Samples from the inner caldera are younger and more differentiated, reflecting

eruptions in 3500 B.P. (Heming, 1974). During their petrogenesis, the predominant crystallizing species were shown to be magnetite, clinopyroxene and amphibole (Hohl et al., 2022), making the Rabaul samples ideal candidates to study the interplay of Ti-oxides (magnetite) and amphiboles (and possible amphibole-derived Ti isotope fractionation, Mandl, 2019). The oldest and least differentiated samples from the outer caldera show the lowest δ^{49}Ti values ($-0.013‰ \pm 0.005‰$ and $-0.023‰ \pm 0.018‰$; 95% c.i. $n = 5$) that are even lower than the range of MORBs and the peridotitic mantle (δ^{49}Ti$_{MORB}$ = $+0.011‰ \pm 0.009‰$ (95% c.i.); Deng et al., 2019; Millet et al., 2016). Nevertheless, as the δ^{49}Ti in the primitive outer caldera samples broadly overlap the mantle value, the Ti in New Britain samples most likely originates from the mantle wedge. Hoare et al. (2020) introduced the parameter $-\ln f$Ti, which describes the fraction of Ti remaining in the melt during differentiation according to:

$$-\ln f\,(\mathrm{Ti}) = -\ln\left(\frac{\left(^{[\mathrm{Ti}]}/_{[\mathrm{incombatible\ element}]}\right)_{\mathrm{sample}}}{\left(^{[\mathrm{Ti}]}/_{[\mathrm{incombatible\ element}]}\right)_{\mathrm{most\ primitive\ sample}}} \right) \tag{9}$$

Thorium is chosen due to its highly incompatible behavior during partial melting (Hoare et al., 2020). The resulting value relates the Ti/Th of a sample to the Ti/Th of the most primitive sample that may represent the initial composition of the melt. For enhanced readability, the negative natural logarithm of fTi ($-\ln(f$Ti)) is used, which is 0 (here: SHR14) for the most primitive sample. With the ongoing fractional crystallization of Ti-bearing minerals, $-\ln(f$Ti) increases (Figure 6a).

Hoare et al. (2020) showed that calc-alkaline igneous rocks from Santorini display different slopes in δ^{49}Ti versus $-\ln(f$Ti) that were interpreted to reflect the fractional crystallization of different oxide minerals. For example, the fractional crystallization of magnetite (or rather a solid solution close to magnetite composition; Buddington & Lindsley, 1964) during the initial stages of differentiation results in a relatively flat slope in δ^{49}Ti versus $-\ln(f$Ti). In contrast, the fractional crystallization of ilmenite and titano-magnetite (or, again, rather a solid solution close to titano-magnetite-/ilmenite-like composition; Buddington & Lindsley, 1964) during later stages of differentiation results in a steeper slope in δ^{49}Ti versus $-\ln(f$Ti). In this context, lavas from Rabaul show the same overall pattern as the Santorini lavas (Figure 6a). While the outer caldera samples show invariant δ^{49}Ti and the smallest amount of Ti extracted from a hypothetical parental melt ($-\ln(f$Ti) close to 0, Figure 6a), $-\ln(f$Ti) and δ^{49}Ti initially increase with a distinct slope of $+0.141 \pm 0.016$ up until a $-\ln(f$Ti) value of 1.2. At higher $-\ln(f$Ti) values, the slope increases to $+0.511 \pm 0.036$ (Figure 6a). Consistent with the results of Hoare et al. (2020), these changing slopes in δ^{49}Ti versus $-\ln(f$Ti) might therefore reflect the transition from a Ti-poor melt (fractional crystallization of oxides akin to magnetite-like compositions) to a Ti-rich melt (fractional crystallization of titano-magnetite- and ilmenite-like compositions; Figure 6a). Interestingly, two samples from the inner caldera (SHR24 and SHR31, Figure 6a) lie outside the δ^{49}Ti versus $-\ln(f$Ti) trend defined by the other samples. Rather, these samples seem to fall on an extrapolated regression line of outer caldera samples. Moreover, the grade of differentiation of respective inner caldera samples is rather similar when compared to outer caldera samples. This may indicate occasional injection of magma originating from the outer caldera magma chamber into the younger caldera (Hohl et al., 2022).

The transition from fractional crystallization of magnetite toward the combined fractional crystallization of titano-magnetite and ilmenite (Figure 6a) would also change the bulk partition coefficient of V ($D_{\mathrm{iV}}^{\mathrm{Imentie-melt}} \sim 1$; Klemme et al., 2006; $D_{\mathrm{V}}^{\mathrm{high-Ti-magnetite-melt}} \sim 40$; Sievwright et al., 2017), whereas the partition coefficient of Ti would remain rather constant ($D_{\mathrm{Ti}}^{\mathrm{ilmenite-melt}} \sim 18$; Klemme et al., 2006; $D_{\mathrm{Ti}}^{\mathrm{high-Ti\,magnetite-melt}} \sim 17$; Sievwright et al., 2017). Thus, the Ti/V ratio should be sensitive to an increased ilmenite component. In the δ^{49}Ti versus Ti/V pattern, we indeed observe a change in the slope from $\sim 0.0145 \pm 0.0006$ to $\sim 0.0041 \pm 0.0003$ (Figure 6b). This change in the slope is consistent with more efficient Ti removal and larger Ti isotope fractionation with the onset of crystallization of oxides close to ilmenite-like compositions.

The discrepancy between the Santorini and our Rabaul suite may point toward an additional phase: Ulmer et al. (2018) constrain the crystallizing phases over the course of calc-alkaline differentiation, which comprise varying amounts of olivine, clino- and orthopyroxene as well as Ti-oxides (represented by magnetite and late stage ilmenite) and amphiboles (see also: Marxer et al., 2022; Nandedkar et al., 2014). These experimental mineral modes are consistent with observations from Woodhead et al. (1998; early onset of (Fe-)Ti-oxide (and amphibole) crystallization) and relevant trace element information from Hohl et al. (2022; Dy/Yb, Ti/V). These mineral modes were fitted against the fraction of remaining liquid using polynomial regressions so that 1% crystallization steps can be extrapolated. For a summary of mineral modes, used mineral-melt partitioning coefficients and fractionation factors, see Table S1 in Supporting Information S1 for the model, see Table S7 in Supporting Information S2.
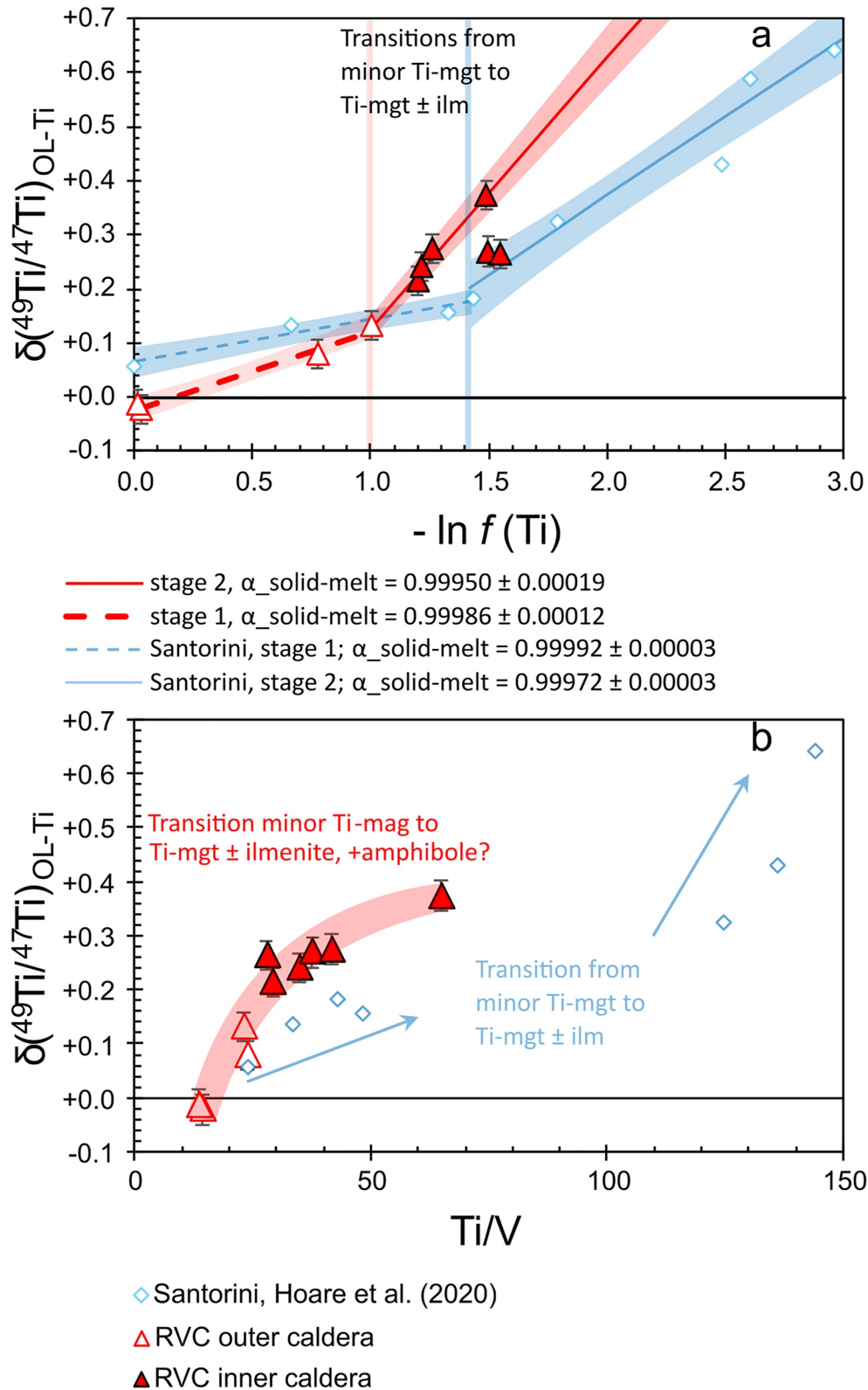
Figure 6.

Titanium, V, Dy, and Yb concentrations were calculated using a fractional crystallization model; Nb and Ta were modeled for reference in Section 5.2 but are shown in the previous section as a case study with no involvement of rutile in the petrogenetic (Equation 9).

$$c_l = c_0 \cdot F^{(D_{bulk}-1)} \tag{10}$$

The observed coeval fractionation of amphibole and the Ti oxide mandates that both phases be included in the calculation of $\Delta^{49}Ti_{bulk\text{-}melt}$, together with both clino- and orthopyroxenes. Three sub-models address the early onset of oxides, where the individual oxides are assumed to be (a) magnetite, (b) titanomagnetite, and (c) ilmenite. The individual Ti contents in the minerals in (a) and (b) are calculated via the $D^{Ti}_{oxide-melt}$ of magnetite and titanomagnetite (Sievwright et al., 2017) and thus allow the application of Hoare et al. (2022) calibration of Ti oxides as well as the ilmenite. As we do not have information on the mole fraction of ülvospinel, we have to rely on TiO$_2$ content alone and use $\Delta^{49}Ti_{titanomagnetite-melt}$ in model (a) and (b).

$$\Delta^{49}Ti_{titanomagnetite-melt} \cong 1{,}000 \ln \alpha_{titanomagnetite-melt} = [-0.0482 \cdot TiO_2 \pm 0.0530] \cdot 10^6/T^2 \tag{11}$$

$$\Delta^{49}Ti_{ilmenite-melt} \cong 1{,}000 \ln \alpha_{ilmenite-melt} = -0.5996 \cdot 10^6/T^2 \tag{12}$$

$$\Delta^{49}Ti_{amphibole-melt} \cong 1{,}000 \ln \alpha_{amphibole-melt} = -0.210 \cdot 10^6/T^2 \tag{13}$$

Additional $\Delta^{49}Ti_{clinopyroxene\text{-}melt}$, $\Delta^{49}Ti_{orthopyroxene\text{-}melt}$ (−0.035‰ and −0.005‰; Rzehak et al., 2021, 2022), and $\Delta^{49}Ti_{amphibole\text{-}melt}$ (−0.05‰; Storck et al., 2023) complete the inventory. The individual $\Delta^{49}Ti_{mineral\text{-}melt}$ were weighed according to their mineral modes and the Ti isotope composition of the melt was then calculated assuming a simple Rayleigh distillation (Equation 1, used in Section 5.1). Calculations are stopped at 80% fractional crystallization ($F = 0.80$).

The partition coefficients for Ti and V for both magnetite species lead to Ti/V that far exceed the observed range, only ilmenite seems to reproduce the observed ranges of Ti/V and $\delta^{49}Ti$ (Figure 7a). Similarly, the Ti extraction (expressed via $-\ln f$ (Ti), Figure 7c), coupled with $\delta^{49}Ti$ fits better with ilmenite than the magnetite species (Figures 7a and 7c). The same can be observed in $\delta^{49}Ti$ versus Dy/Yb (Figure 7b); the magnetite and titanomagnetite models end up to low with respect to their $\delta^{49}Ti$. After a slight increase in mineral modes for amphibole and ilmenite (by a factor of 1.7 and 1.2 respectively), ilmenite and amphibole do seem to be the best fit. Using the value by Storck et al. (2023) reproduces lower $\Delta^{49}Ti_{bulk\text{-}melt}$ values and thus leads to slightly lower $\delta^{49}Ti$. The observed change in the α value (in $\delta^{49}Ti$ vs. $-\ln f$ (Ti), from 0.99986 to 0.99950, Figure 7c) is not reproduced with experimental mineral modes and neither is the highest $\delta^{49}Ti$ in our sample set (SHR32). Changing these mineral modes to better fit the $\delta^{49}Ti$ versus $-\ln f$ (Ti) would drastically change the observed trace element ratios; therefore, both mineral modes and partitioning data seem to be accurate; therefore, the issue is likely related to non-ideal Ti partitioning data. Given the constraints of mineral modes, partitioning data and $\Delta^{49}Ti_{Ti\text{-}oxide\text{-}melt}$, $\Delta^{49}Ti_{amphibole\text{-}melt}$ is the parameter with the largest ambiguity: While there is consensus on the influence of amphibole on Ti content and Ti isotope fractionation in calc-alkaline systems, the extent of this influence is still being investigated (Greber et al., 2021; Mandl, 2019; Storck et al., 2023). The highest $\delta^{49}Ti$ in the Rabaul samples (SHR32) were only reached when altering the $\Delta^{49}Ti_{amphibole\text{-}melt}$ toward lower values (from $\Delta^{49}Ti_{amphibole\text{-}melt} = -0.210 \times 10^6/T^2$ to $= -0.50 \times 10^6/T^2$ and below) which is pure speculation. In that context, Marxer et al. (2022) observe increased compatibility of Ti in amphibole with increasing presence of ilmenite and decreasing temperature, wherein the increased compatibility of Ti in amphibole is interpreted as a Ti-Tschermak exchange reaction. This may point toward $\Delta^{49}Ti_{amphibole\text{-}melt}$ being a function of fO_2 (affecting ilmenite stability) and/or TiO$_2$ in addition to temperature, similar to the codependency of $\Delta^{49}Ti_{titanomagnetite\text{-}melt}$ and TiO$_2$ content as observed by Hoare et al. (2022). While our data strongly support the notion that amphiboles have a significant impact on the Ti isotope composition of differentiation calc-alkaline arc basalts, the exact impact goes beyond the scope of this paper.

Nevertheless, the observed pattern in $\delta^{49}Ti$ versus Ti/V, $\delta^{49}Ti$ versus Dy/Yb (Figures 7a and 7b) can best be modeled assuming fractional crystallization of both ilmenite and amphibole. These observations are broadly

Figure 6. Titanium isotope composition relative to panel (a) $-\ln f$ Ti (the negative logarithm of the fraction of Ti remaining in the sample relative to the most primitive sample SHR14 = 0, see text and Equation 6) and panel (b) Ti/V (trace element data from Hohl et al., 2022). Data for samples from Santorini with the corresponding bulk-melt fractionation factors (±95% c.i.) by Hoare et al. (2020), the vertical blue and red lines in (a) marks the postulated transition in crystallizing phases from Ti-magnetite (Ti-mgt) to Ti-magnetite and ilmenite (ilm) in two suites. The apparent similarity of Rabaul and Santorini no longer holds true when Ti/V is considered (inversion of the observed trends), suggesting the presence of an additional phase, potentially amphiboles (amph).
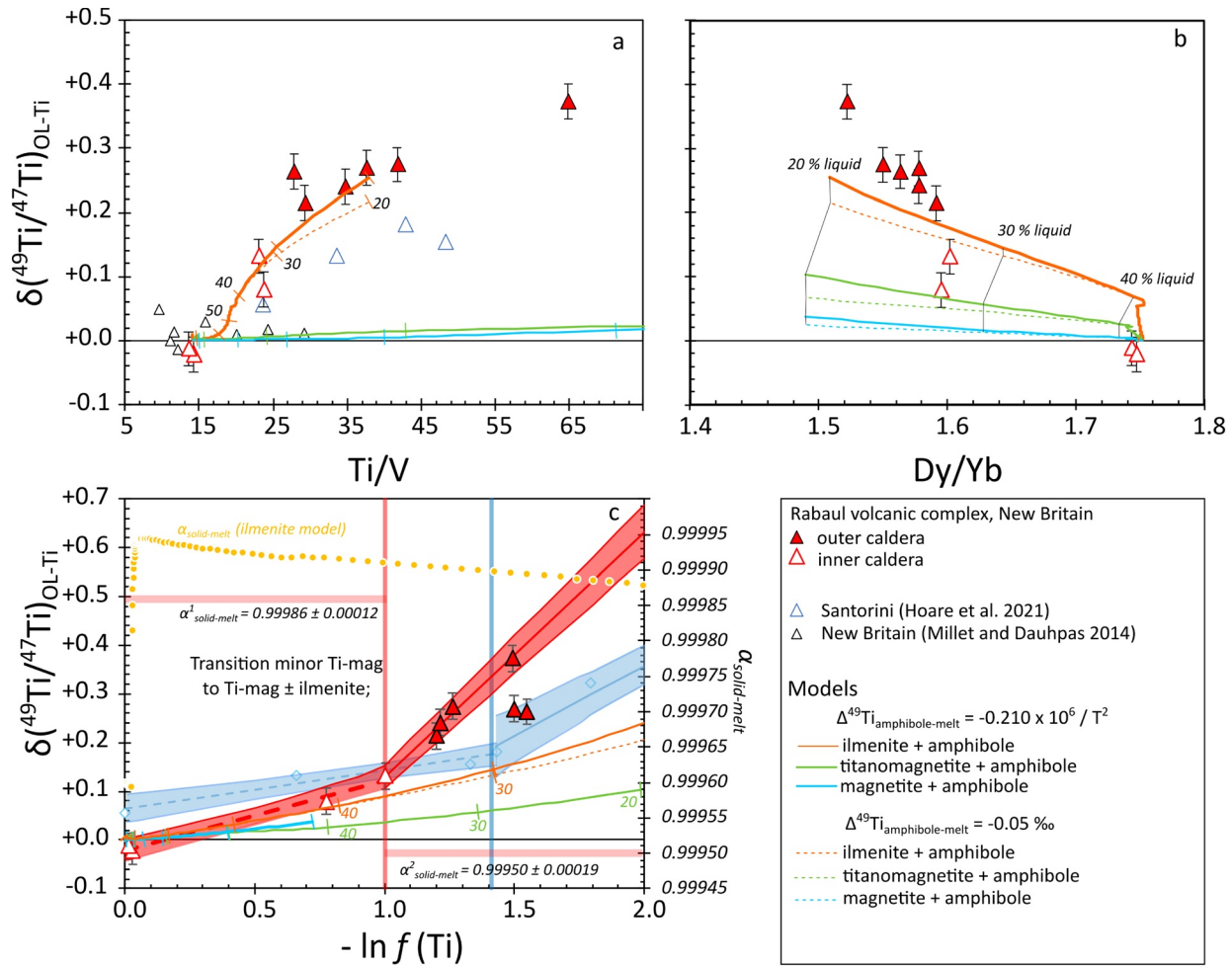
Figure 7. (a–c) Modeled δ^{49}Ti and Ti/V (panel a), δ^{49}Ti versus Dy/Yb (panel b) and δ^{49}Ti versus $-\ln f$ (Ti) compared to the compositions of the analyzed samples and literature data. Panel c additionally shows the modeled bulk alpha and the alfa from the regressions on a secondary y-axis (shaded areas, see also the figure). a^1 and ^{2} represent the a-values determined in this figure. Solid lines represent models using one type of oxide and Δ^{49}Ti$_{amphibole-melt}$ from Mandl (2019), dashed lines (if shown) utilize the Δ^{49}Ti$_{amphibole-melt}$ used in Storck et al. (2023). Number close to tick marks represents the amount of liquid remaining, in panel b individual marks have been connected via thin black lines for better visibility. The magnetite models using both Δ^{49}Ti$_{amphibole-melt}$ only significantly diverge in δ^{49}Ti versus Dy/Yb and are thus not shown in panels (a) and (c).

consistent with findings by Hohl et al. (2022), specifically the presence of Ti-oxide and amphibole phenocrysts and their influence on the trace element budget (and Fe stable isotope variations) of Rabaul samples. Furthermore, significant Ti isotope fractionation during fractional crystallization of ilmenite and amphibole with fractionation factors in the range of previous estimates by Mandl (2019) is required. While ambiguities remain that need addressing, our results strongly suggest a potential impact of amphiboles on the Ti stable isotope fractionation of a suite of calc-alkaline igneous rocks.

6. Conclusions

New Ti isotope data for subduction-related lavas from different petrogenetic settings confirm that fractional crystallization of Ti-rich oxides exerts the main control on the Ti isotope composition of igneous rocks. In the absence of fractional crystallization of Ti-rich oxides (or amphibole), the Ti budget of the melt is controlled by source processes that have small impacts on the Ti isotope composition (i.e., partial melting of a variably depleted peridotitic mantle and addition of subduction components). In our study, the contributions of components derived from subducted pelagic sediment melts (Cyprus, Sunda arc) barely change the Ti isotope composition of the melt, although sediments are often distinctly heavier in their Ti isotope composition compared to basaltic rocks. Rather,

in highly depleted mantle sources like those of boninites (Cyprus and Papua New Guinea), residual Cr-spinel can control Ti isotope fractionation. We note that the addition of subduction components with residual rutile (Solomon Islands, Sunda rear arc) can potentially cause minor but still resolvable variation in Ti isotope compositions. Our study further tentatively shows for the first time that fractional crystallization of amphiboles also significantly affects the Ti isotope composition of lavas, while fractional crystallization of olivine and pyroxene is negligible. This, in combination with observations made from crystallization experiments may point toward a codependency of Ti-content in amphibole and the $\Delta^{49}Ti_{amphibole-melt}$.

Data Availability Statement

Major and trace element data used in this study are published in Fonseca et al. (2017), Hohl et al. (2022), Kirchenbaur and Münker (2015), Kirchenbaur et al. (2022), König et al. (2008), König et al. (2010), Kurzweil et al. (2019), and Schuth et al. (2009) and can be found additionally in Supporting Information S1, with appropriate references and their corresponding Titanium isotope compositions. Titanium isotope data are archived at Kommescher et al. (2023).

References

Aarons, S. M., Dauphas, N., Blanchard, M., Zeng, H., Nie, N. X., Johnson, A. C., et al. (2021). Clues from *Ab initio* calculations on titanium isotopic fractionation in tholeiitic and calc-alkaline magma series. *ACS Earth and Space Chemistry, acsearthspacechem, 5*(9), 1c00172–2480. https://doi.org/10.1021/acsearthspacechem.1c00172

Adam, J., & Green, T. (2006). Trace element partitioning between mica- and amphibole-bearing garnet lherzolite and hydrous basanitic melt: 1. Experimental results and the investigation of controls on partitioning behaviour. *Contributions to Mineralogy and Petrology, 152*(1), 1–17. https://doi.org/10.1007/s00410-006-0085-4

Alderman, O. L. G., Skinner, L. B., Benmore, C. J., Tamalonis, A., & Weber, J. K. R. (2014). Structure of molten titanium dioxide. *Physical Review B, 90*(9), 094204. https://doi.org/10.1103/PhysRevB.90.094204

Anguelova, M., Fehr, M. A., Takazawa, E., & Schönbächler, M. (2022). Titanium isotope heterogeneity in the Earth's mantle: A case study of the Horoman peridotite massif. *Geochimica et Cosmochimica Acta, 335*, 356–368. https://doi.org/10.1016/j.gca.2022.07.005

Bednarz, U., & Schmincke, H.-U. (1989). Mass transfer during sub-seafloor alteration of the upper Troodos crust (Cyprus). *Contributions to Mineralogy and Petrology, 102*(1), 93–101. https://doi.org/10.1007/BF01160193

Bodinier, J.-L., & Godard, M. (2014). Orogenic, ophiolitic, and Abyssal peridotites. In *Treatise on geochemistry* (pp. 103–167). Elsevier. https://doi.org/10.1016/B978-0-08-095975-7.00204-7

Buddington, A. F., & Lindsley, D. H. (1964). Iron-Titanium oxide minerals and synthetic equivalents. *Journal of Petrology, 5*(2), 310–357. https://doi.org/10.1093/petrology/5.2.310

Cameron, W. E., McCulloch, M. T., & Walker, D. A. (1983). Boninite petrogenesis: Chemical and Nd-Sr isotopic constraints. *Earth and Planetary Science Letters, 65*(1), 75–89. https://doi.org/10.1016/0012-821X(83)90191-7

Compston, W., & Oversby, V. M. (1969). Lead isotopic analysis using a double spike. *Journal of Geophysical Research, 74*(17), 4338–4348. https://doi.org/10.1029/JB074i017p04338

Crawford, A. J., Falloon, T., & Green, D. (1989). Classification, petrogenesis and tectonic setting of boninites. *Boninites and Related Rocks*, 1–49.

David, K., Schiano, P., & Allègre, C. J. (2000). Assessment of the Zr/Hf fractionation in oceanic basalts and continental materials during petrogenetic processes. *Earth and Planetary Science Letters, 178*(3–4), 285–301. https://doi.org/10.1016/S0012-821X(00)00088-1

Davidson, J., Turner, S., Handley, H., Macpherson, C., & Dosseto, A. (2007). Amphibole "sponge" in arc crust? *Geology, 35*(9), 787. https://doi.org/10.1130/G23637A.1

Deng, Z., Chaussidon, M., Savage, P., Robert, F., Pik, R., & Moynier, F. (2019). Titanium isotopes as a tracer for the plume or island arc affinity of felsic rocks. *Proceedings of the National Academy of Sciences, 116*(4), 1132–1135. https://doi.org/10.1073/pnas.1809164116

DePaolo, D. J., & Johnson, R. W. (1979). Magma Genesis in the New Britain island-arc: Constraints from Nd and Sr isotopes and trace-element patterns. *Contributions to Mineralogy and Petrology, 70*(4), 367–379. https://doi.org/10.1007/BF00371044

Elkins, L. J., Gaetani, G. A., & Sims, K. W. W. (2008). Partitioning of U and Th during garnet pyroxenite partial melting: Constraints on the source of alkaline ocean island basalts. *Earth and Planetary Science Letters, 17*(1–2), 270–286. https://doi.org/10.1016/j.epsl.2007.10.034

Farges, F., Brown, G. E., Navrotsky, A., Gan, H., & Rehr, J. J. (1996a). Coordination chemistry of Ti(IV) in silicate glasses and melts: II. Glasses at ambient temperature and pressure. *Geochimica et Cosmochimica Acta, 60*(16), 3039–3053. https://doi.org/10.1016/0016-7037(96)00145-7

Farges, F., Brown, G. E., Navrotsky, A., Gan, H., & Rehr, J. R. (1996b). Coordination chemistry of Ti(IV) in silicate glasses and melts: III. Glasses and melts from ambient to high temperatures. *Geochimica et Cosmochimica Acta, 60*(16), 3055–3065. https://doi.org/10.1016/0016-7037(96)00146-9

Farges, F., Brown, G. E., & Rehr, J. J. (1996). Coordination chemistry of Ti(IV) in silicate glasses and melts: I. XAFS study of titanium coordination in oxide model compounds. *Geochimica et Cosmochimica Acta, 60*(16), 3023–3038. https://doi.org/10.1016/0016-7037(96)00144-5

Foley, S., Tiepolo, M., & Vannucci, R. (2002). Growth of early continental crust controlled by melting of amphibolite in subduction zones. *Nature, 417*(6891), 837–840. https://doi.org/10.1038/nature00799

Fonseca, R. O. C., Kirchenbaur, M., Ballhaus, C., Münker, C., Zirner, A., Gerdes, A., et al. (2017). Fingerprinting fluid sources in Troodos ophiolite complex orbicular glasses using high spatial resolution isotope and trace element geochemistry. *Geochimica et Cosmochimica Acta, 200*, 145–166. https://doi.org/10.1016/j.gca.2016.12.012

Gertisser, R. (2003). Trace element and Sr, Nd, Pb and O isotope variations in medium-K and high-K volcanic rocks from merapi volcano, Central Java, Indonesia: Evidence for the involvement of subducted sediments in Sunda Arc magma Genesis. *Journal of Petrology, 44*(3), 457–489. https://doi.org/10.1093/petrology/44.3.457

Greber, N. D., Dauphas, N., Bekker, A., Ptáček, M. P., Bindeman, I. N., & Hofmann, A. (2017). Titanium isotopic evidence for felsic crust and plate tectonics 3.5 billion years ago. *Science, 357*(6357), 1271–1274. https://doi.org/10.1126/science.aan8086

Greber, N. D., Pettke, T., Vilela, N., Lanari, P., & Dauphas, N. (2021). Titanium isotopic compositions of bulk rocks and mineral separates from the Kos magmatic suite: Insights into fractional crystallization and magma mixing processes. *Chemical Geology*, *578*, 120303. https://doi.org/10.1016/j.chemgeo.2021.120303

Green, T. H., & Pearson, N. J. (1986). Ti-rich accessory phase saturation in hydrous mafic-felsic compositions at high P,T. *Chemical Geology*, *54*(3–4), 185–201. https://doi.org/10.1016/0009-2541(86)90136-1

Gualda, G. A. R., & Ghiorso, M. S. (2015). MELTS_Excel: AMicrosoft excel-based MELTS interface for research and teaching of magma properties and evolution. *Geochemistry, Geophysics, Geosystems*, *16*(1), 315–324. https://doi.org/10.1002/2014GC005545

Hall, R. (2002). Cenozoic geological and plate tectonic evolution of SE Asia and the SW Paci®c: Computer-based reconstructions, model and animations. *Journal of Asian Earth Sciences*, *79*, 353.

Hamilton, W. (1979). Tectonics of the Indonesian region. In *USGS numbered series, professional paper (1078)* (p. 356). https://doi.org/10.3133/pp1078

Handley, H. K., Turner, S., Macpherson, C. G., Gertisser, R., & Davidson, J. P. (2011). Hf–Nd isotope and trace element constraints on subduction inputs at island arcs: Limitations of Hf anomalies as sediment input indicators. *Earth and Planetary Science Letters*, *304*(1–2), 212–223. https://doi.org/10.1016/j.epsl.2011.01.034

Handley, H. K., Blichert-Toft, J., Gertisser, R., Macpherson, C. G., Turner, S. P., Zaennudin, A., & Abdurrachman, M. (2014). Insights from Pb and O isotopes into along-arc variations in subduction inputs and crustal assimilation for volcanic rocks in Java, Sunda arc, Indonesia. *Geochimica et Cosmochimica Acta*, *139*, 205–226. https://doi.org/10.1016/j.gca.2014.04.025

Handley, H. K., Macpherson, C. G., Davidson, J. P., Berlo, K., & Lowry, D. (2007). Constraining fluid and sediment contributions to subduction-related magmatism in Indonesia: Ijen volcanic complex. *Journal of Petrology*, *48*(6), 1155–1183. https://doi.org/10.1093/petrology/egm013

Hawkesworth, C., Turner, S., Peate, D., McDermott, F., & van Calsteren, P. (1997). Elemental U and Th variations in island arc rocks: Implications for U-series isotopes. *Chemical Geology*, *139*(1–4), 207–221. https://doi.org/10.1016/S0009-2541(97)00036-3

Hawkins, J. W., Bloomer, S. H., Evans, C. A., & Melchior, J. T. (1984). Evolution of intra-oceanic arc-trench systems. *Tectonophysics*, *102*(1–4), 175–205. https://doi.org/10.1016/0040-1951(84)90013-1

He, X., Ma, J., Wei, G., Zhang, L., Wang, Z., & Wang, Q. (2020). A new procedure for titanium separation in geological samples for $^{49}Ti/^{47}Ti$ ratio measurement by MC-ICP-MS. *Journal of Analytical Atomic Spectrometry*, *35*(1), 100–106. https://doi.org/10.1039/C9JA00316A

Heming, R. F. (1974). Geology and petrology of Rabaul caldera, Papua New Guinea. *GSA Bulletin*, *85*(8), 1253–1264. https://doi.org/10.1130/0016-7606(1974)85<1253:GAPORC>2.0.CO;2

Hermann, J., & Rubatto, D. (2009). Accessory phase control on the trace element signature of sediment melts in subduction zones. *Chemical Geology*, *265*(3–4), 512–526. https://doi.org/10.1016/j.chemgeo.2009.05.018

Heuser, A., Eisenhauer, A., Gussone, N., Bock, B., Hansen, B. T., & Nägler, T. F. (2002). Measurement of calcium isotopes ($\delta^{44}Ca$) using a multi-collector TIMS technique. *International Journal of Mass Spectrometry*, *220*(3), 385–397. https://doi.org/10.1016/S1387-3806(02)00838-2

Hoare, L., Klaver, M., Muir, D. D., Klemme, S., Barling, J., Parkinson, I. J., et al. (2022). Empirical and experimental constraints on Fe-Ti oxide-melt titanium isotope fractionation factors. *Geochimica et Cosmochimica Acta*, *326*, 253–272. https://doi.org/10.1016/j.gca.2022.02.011

Hoare, L., Klaver, M., Saji, N. S., Gillies, J., Parkinson, I. J., Lissenberg, C. J., & Millet, M.-A. (2020). Melt chemistry and redox conditions control titanium isotope fractionation during magmatic differentiation. *Geochimica et Cosmochimica Acta*, *282*, 38–54. https://doi.org/10.1016/j.gca.2020.05.015

Hohl, S. V., Schuth, S., Münker, C., König, S., Garbe-Schönberg, D., & Kuduon, J. (2022). Geochemical evolution of the Rabaul volcanic complex, Papua New Guinea—Insights from HFSE, Sr-Nd-Hf, and Fe isotopes. *Lithos*, *408–409*, 106560. https://doi.org/10.1016/j.lithos.2021.106560

Jaques, A. L., & Chappell, B. W. (1980). Petrology and trace element geochemistry of the papuan ultramafic belt. *Contributions to Mineralogy and Petrology*, *75*(1), 55–70. https://doi.org/10.1007/bf00371889

Johnson, A. C., Aarons, S. M., Dauphas, N., Nie, N. X., Zeng, H., Helz, R. T., et al. (2019). Titanium isotopic fractionation in Kilauea Iki lava lake driven by oxide crystallization. *Geochimica et Cosmochimica Acta*, *264*, 180–190. https://doi.org/10.1016/j.gca.2019.08.022

Joshima, M., Okuda, Y., Murakami, F., Kishimoto, K., & Honza, E. (1986). Age of the Solomon Sea Basin from magnetic lineations. *Geo-Marine Letters*, *6*(4), 229–234. https://doi.org/10.1007/BF02239584

Katili, J. A. (1975). Volcanism and plate tectonics in the Indonesian island arcs. *Tectonophysics*, *26*(3–4), 165–188. https://doi.org/10.1016/0040-1951(75)90088-8

Kessel, R., Schmidt, M. W., Ulmer, P., & Pettke, T. (2005). Trace element signature of subduction-zone fluids, melts and supercritical liquids at 120–180 km depth. *Nature*, *437*(7059), 724–727. https://doi.org/10.1038/nature03971

Kirchenbaur, M., & Münker, C. (2015). The behaviour of the extended HFSE group (Nb, Ta, Zr, Hf, W, Mo) during the petrogenesis of mafic K-rich lavas: The Eastern Mediterranean case. *Geochimica et Cosmochimica Acta*, *165*, 178–199. https://doi.org/10.1016/j.gca.2015.05.030

Kirchenbaur, M., Schuth, S., Barth, A. R., Luguet, A., König, S., Idrus, A., et al. (2022). Sub-arc mantle enrichment in the Sunda rear-arc inferred from HFSE systematics in high-K lavas from Java. *Contributions to Mineralogy and Petrology*, *177*(1), 8. https://doi.org/10.1007/s00410-021-01871-9

Klaver, M., Djuly, T., de Graaf, S., Sakes, A., Wijbrans, J., Davies, G., & Vroon, P. (2015). Temporal and spatial variations in provenance of Eastern mediterranean Sea sediments: Implications for Aegean and Aeolian arc volcanism. *Geochimica et Cosmochimica Acta*, *153*, 149–168. https://doi.org/10.1016/j.gca.2015.01.007

Klaver, M., MacLennan, S. A., Ibañez-Mejia, M., Tissot, F. L. H., Vroon, P. Z., & Millet, M.-A. (2021). Reliability of detrital marine sediments as proxy for continental crust composition: The effects of hydrodynamic sorting on Ti and Zr isotope systematics. *Geochimica et Cosmochimica Acta*, *310*, 221–239. https://doi.org/10.1016/j.gca.2021.05.030

Klemme, S., Blundy, J. D., & Wood, B. J. (2002). Experimental constraints on major and trace element partitioning during partial melting of eclogite. *Geochimica et Cosmochimica Acta*, *66*(17), 3109–3123. https://doi.org/10.1016/S0016-7037(02)00859-1

Klemme, S., Günther, D., Hametner, K., Prowatke, S., & Zack, T. (2006). The partitioning of trace elements between ilmenite, ulvospinel, armalcolite and silicate melts with implications for the early differentiation of the moon. *Chemical Geology*, *234*(3–4), 251–263. https://doi.org/10.1016/j.chemgeo.2006.05.005

Klemme, S., Prowatke, S., Hametner, K., & Günther, D. (2005). Partitioning of trace elements between rutile and silicate melts: Implications for subduction zones. *Geochimica et Cosmochimica Acta*, *69*(9), 2361–2371. https://doi.org/10.1016/j.gca.2004.11.015

Kommescher, S., Fonseca, R. O. C., Kurzweil, F., Thiemens, M. M., Münker, C., & Sprung, P. (2020). Unravelling lunar mantle source processes via the Ti isotope composition of lunar basalts. *Geochemical Perspectives Letters*, *13*, 13–18. https://doi.org/10.7185/geochemlet.2007

Kommescher, S., Kurzweil, F., Fonseca, R. O. C., Rzehak, L. J. A., Hohl, S. V., Kirchenbaur, M., et al. (2023). Mineralogical controls on the Ti isotope composition of subduction zone magmas (Version 1.0) [Dataset]. Interdisciplinary Earth Data Alliance (IEDA). https://doi.org/10.26022/IEDA/112936

König, S., Münker, C., Schuth, S., & Garbe-Schönberg, D. (2008). Mobility of tungsten in subduction zones. *Earth and Planetary Science Letters*, *274*(1–2), 82–92. https://doi.org/10.1016/j.epsl.2008.07.002

König, S., Münker, C., Schuth, S., Luguet, A., Hoffmann, J. E., & Kuduon, J. (2010). Boninites as windows into trace element mobility in subduction zones. *Geochimica et Cosmochimica Acta*, *74*(2), 684–704. https://doi.org/10.1016/j.gca.2009.10.011

König, S., & Schuth, S. (2011). Deep melting of old subducted oceanic crust recorded by superchondritic Nb/Ta in modern island arc lavas. *Earth and Planetary Science Letters*, *10*(1–2), 265–274. https://doi.org/10.1016/j.epsl.2010.11.007

Kurzweil, F., Münker, C., Grupp, M., Braukmüller, N., Fechtner, L., Christian, M., et al. (2019). The stable tungsten isotope composition of modern igneous reservoirs. *Geochimica et Cosmochimica Acta*, *251*, 176–191. https://doi.org/10.1016/j.gca.2019.02.025

Leitzke, F. P., Fonseca, R. O. C., Michely, L. T., Sprung, P., Münker, C., Heuser, A., & Blanchard, H. (2016). The effect of titanium on the partitioning behavior of high-field strength elements between silicates, oxides and lunar basaltic melts with applications to the origin of mare basalts. *Chemical Geology*, *440*, 219–238. https://doi.org/10.1016/j.chemgeo.2016.07.011

Mandl, M. B. (2019). Titanium isotope fractionation on the Earth and Moon: Constraints on magmatic processes and Moon formation (Application/pdf). *ETH Zurich*. https://doi.org/10.3929/ETHZ-B-000351171

Marxer, F., Ulmer, P., & Müntener, O. (2022). Polybaric fractional crystallisation of arc magmas: An experimental study simulating trans-crustal magmatic systems. *Contributions to Mineralogy and Petrology*, *177*(1), 3. https://doi.org/10.1007/s00410-021-01856-8

McDonough, W. F., Stosch, H.-G., & Ware, N. G. (1992). Distribution of titanium and the rare Earth elements between peridotitic minerals. *Contributions to Mineralogy and Petrology*, *110*(2–3), 321–328. https://doi.org/10.1007/BF00310747

McKee, C. O. (2015). Tavui Volcano: Neighbour of Rabaul and likely source of the middle Holocene penultimate major eruption in the Rabaul area. *Bulletin of Volcanology*, *21*(9), 80. https://doi.org/10.1007/s00445-015-0968-1

Meinhold, G. (2010). Rutile and its applications in Earth sciences. *Earth-Science Reviews*, *102*(1–2), 1–28. https://doi.org/10.1016/j.earscirev.2010.06.001

Millet, M.-A., & Dauphas, N. (2014). Ultra-precise titanium stable isotope measurements by double-spike high resolution MC-ICP-MS. *Journal of Analytical Atomic Spectrometry*, *29*(8), 1444. https://doi.org/10.1039/C4JA00096J

Millet, M.-A., Dauphas, N., Greber, N. D., Burton, K. W., Dale, C. W., Debret, B., et al. (2016). Titanium stable isotope investigation of magmatic processes on the Earth and Moon. *Earth and Planetary Science Letters*, *449*, 197–205. https://doi.org/10.1016/j.epsl.2016.05.039

Mills, K. C. (1993). The influence of structure on the physico-chemical properties of slags. *ISIJ International*, *33*(1), 148–155. https://doi.org/10.2355/isijinternational.33.148

Münker, C., Wörner, G., Yogodzinski, G., & Churikova, T. (2004). Behaviour of high field strength elements in subduction zones: Constraints from Kamchatka–Aleutian arc lavas. *Earth and Planetary Science Letters*, *224*(3–4), 275–293. https://doi.org/10.1016/j.epsl.2004.05.030

Mysen, B., & Richet, P. (2019). Titanium-bearing systems. In *Silicate glasses and melts* (pp. 431–466). Elsevier. https://doi.org/10.1016/B978-0-444-63708-6.00012-0

Nandedkar, R. H., Ulmer, P., & Müntener, O. (2014). Fractional crystallization of primitive, hydrous arc magmas: An experimental study at 0.7 GPa. *Contributions to Mineralogy and Petrology*, *167*(6), 1015. https://doi.org/10.1007/s00410-014-1015-5

Nie, N. X., Dauphas, N., Alp, E. E., Zeng, H., Sio, C. K., Hu, J. Y., et al. (2021). Iron, magnesium, and titanium isotopic fractionations between garnet, ilmenite, fayalite, biotite, and tourmaline: Results from NRIXS, ab initio, and study of mineral separates from the Moosilauke metapelite. *Geochimica et Cosmochimica Acta*, *302*, 18–45. https://doi.org/10.1016/j.gca.2021.03.014

Okube, M., Oshiumi, T., Nagase, T., Miyawaki, R., Yoshiasa, A., Sasaki, S., & Sugiyama, K. (2018). Site occupancy of Fe^{2+}, Fe^{3+} and Ti^{4+} in titanomagnetite determined by valence-difference contrast in synchrotron X-ray resonant scattering. *Journal of Synchrotron Radiation*, *25*(6), 1694–1702. https://doi.org/10.1107/S1600577518013954

Osozawa, S., Shinjo, R., Lo, C.-H., Jahn, B., Hoang, N., Sasaki, M., et al. (2012). Geochemistry and geochronology of the Troodos ophiolite: An SSZ ophiolite generated by subduction initiation and an extended episode of ridge subduction? *Lithosphere*, *4*(6), 497–510. https://doi.org/10.1130/L205.1

Pearce, J. A., Lippard, S. J., & Roberts, S. (1984). Characteristics and tectonic significance of supra-subduction zone ophiolites. *Geological Society, London, Special Publications*, *16*(1), 77–94. https://doi.org/10.1144/GSL.SP.1984.016.01.06

Prytulak, J., & Elliott, T. (2007). TiO_2 enrichment in ocean island basalts. *Earth and Planetary Science Letters*, *263*(3–4), 388–403. https://doi.org/10.1016/j.epsl.2007.09.015

Rapp, R. P., & Watson, E. B. (1995). Dehydration melting of metabasalt at 8–32 kbar: Implications for continental growth and crust-mantle recycling. *Journal of Petrology*, *36*(4), 891–931. https://doi.org/10.1093/petrology/36.4.891

Rautenschlein, M., Jenner, G. A., Hertogen, J., Hofmann, A. W., Kerrich, R., Schmincke, H.-U., & White, W. M. (1985). Isotopic and trace element composition of volcanic glasses from the Akaki Canyon, Cyprus: Implications for the origin of the Troodos ophiolite. *Earth and Planetary Science Letters*, *75*(4), 369–383. https://doi.org/10.1016/0012-821X(85)90180-3

Regelous, M., Haase, K. M., Freund, S., Keith, M., Weinzierl, C. G., Beier, C., et al. (2014). Formation of the Troodos Ophiolite at a triple junction: Evidence from trace elements in volcanic glass. *Chemical Geology*, *386*, 66–79. https://doi.org/10.1016/j.chemgeo.2014.08.006

Rzehak, L. J. A., Kommescher, S., Hoare, L., Kurzweil, F., Sprung, P., Leitzke, F. P., & Fonseca, R. O. C. (2022). Redox-dependent Ti stable isotope fractionation on the moon: Implications for current lunar magma ocean models. *Contributions to Mineralogy and Petrology*, *177*(8), 81. https://doi.org/10.1007/s00410-022-01947-0

Rzehak, L. J. A., Kommescher, S., Kurzweil, F., Sprung, P., Leitzke, F. P., & Fonseca, R. O. C. (2021). The redox dependence of titanium isotope fractionation in synthetic Ti-rich lunar melts. *Contributions to Mineralogy and Petrology*, *176*(3), 19. https://doi.org/10.1007/s00410-020-01769-y

Schauble, E. A. (2004). Applying stable isotope fractionation theory to new systems. *Reviews in Mineralogy and Geochemistry*, *55*(1), 65–111. https://doi.org/10.2138/gsrmg.55.1.65

Schönberg, R., Zink, S., Staubwasser, M., & von Blanckenburg, F. (2008). The stable Cr isotope inventory of solid Earth reservoirs determined by double spike MC-ICP-MS. *Chemical Geology*, *249*(3–4), 294–306. https://doi.org/10.1016/j.chemgeo.2008.01.009

Schuth, S., Münker, C., König, S., Qopoto, C., Basi, S., Garbe-Schönberg, D., & Ballhaus, C. (2009). Petrogenesis of lavas along the Solomon Island Arc, SW Pacific: Coupling of compositional variations and subduction zone geometry. *Journal of Petrology*, *50*(5), 781–811. https://doi.org/10.1093/petrology/egp019

Schuth, S., Rohrbach, A., Ballhaus, C., Qopoto, C., & Garbe-Schönberg, D. (2004). Geochemical constraints on the petrogenesis of arc picrites and basalts, New Georgia Group, Solomon Islands. *Contributions to Mineralogy and Petrology*, *148*(3), 288–304. https://doi.org/10.1007/s00410-004-0604-0

Shaw, D. M. (1970). Trace element fractionation during anatexis. *Geochimica et Cosmochimica Acta*, *34*(2), 237–243. https://doi.org/10.1016/0016-7037(70)90009-8

Shervais, J. W. (1982). Ti-V plots and the petrogenesis of modern and ophiolitic lavas. *Earth and Planetary Science Letters*, *59*(1), 101–118. https://doi.org/10.1016/0012-821X(82)90120-0

Sievwright, R. H., Wilkinson, J. J., O'Neill, H. S. C., & Berry, A. J. (2017). Thermodynamic controls on element partitioning between titanomagnetite and andesitic–dacitic silicate melts. *Contributions to Mineralogy and Petrology*, *172*(8), 62. https://doi.org/10.1007/s00410-017-1385-6

Stolz, A. J., Jochum, K. P., Spettel, B., & Hofmann, A. W. (1996). Fluid- and melt-related enrichment in the subarc mantle: Evidence from Nb/Ta variations in island-arc basalts. *Geology*, *24*(7), 587–590. https://doi.org/10.1130/0091-7613(1996)024<0587:famrei>2.3.co;2

Storck, J.-C., Greber, N. D., Duarte, J. F. V., Lanari, P., Tiepolo, M., & Pettke, T. (2023). Molybdenum and titanium isotopic signatures of arc-derived cumulates. *Chemical Geology*, *617*, 121260. https://doi.org/10.1016/j.chemgeo.2022.121260

Turner, S., & Foden, J. (2001). U, Th and Ra disequilibria, Sr, Nd and Pb isotope and trace element variations in Sunda arc lavas: Predominance of a subducted sediment component. *Contributions to Mineralogy and Petrology*, *142*(1), 43–57. https://doi.org/10.1007/s004100100271

Tusch, J., Sprung, P., van de Löcht, J., Hoffmann, J. E., Boyd, A. J., Rosing, M. T., & Münker, C. (2019). Uniform 182W isotope compositions in Eoarchean rocks from the Isua region, SW Greenland: The role of early silicate differentiation and missing late veneer. *Geochimica et Cosmochimica Acta*, *257*, 284–310. https://doi.org/10.1016/j.gca.2019.05.012

Ulmer, P., Kaegi, R., & Müntener, O. (2018). Experimentally derived intermediate to silica-rich Arc Magmas by fractional and equilibrium crystallization at 1·0 GPa: An evaluation of phase relationships, compositions, liquid lines of descent and oxygen fugacity. *Journal of Petrology*, *59*(1), 11–58. https://doi.org/10.1093/petrology/egy017

van Bemmelen, R. W. (1970). *The geology of Indonesia* (2nd ed.). Martinus Nijhoff.

Walker, D. A., & McDougall, I. (1982). 40Ar/39Ar and K-Ar dating of altered glassy volcanic rocks: The Dabi volcanics, Papua New Guinea. *Geochimica et Cosmochimica Acta*, *46*(11), 2181–2190. https://doi.org/10.1016/0016-7037(82)90193-4

Wang, W., Huang, S., Huang, F., Zhao, X., & Wu, Z. (2020). Equilibrium inter-mineral titanium isotope fractionation: Implication for high-temperature titanium isotope geochemistry. *Geochimica et Cosmochimica Acta*, *269*, 540–553. https://doi.org/10.1016/j.gca.2019.11.008

Weissel, J. K., Taylor, B., & Karner, G. D. (1982). The opening of the Woodlark Basin, subduction of the Woodlark spreading system, and the evolution of Northern Melanesia since mid-pliocene time. *The Evolution of the India-Pacific Plate Boundaries*, *87*(1), 253–277. https://doi.org/10.1016/0040-1951(82)90229-3

Weyer, S., & Schwieters, J. B. (2003). High precision Fe isotope measurements with high mass resolution MC-ICPMS. *International Journal of Mass Spectrometry*, *226*(3), 355–368. https://doi.org/10.1016/S1387-3806(03)00078-2

White, W. M., & Klein, E. M. (2014). Composition of the oceanic crust. In *Treatise on geochemistry* (pp. 457–496). Elsevier. https://doi.org/10.1016/B978-0-08-095975-7.00315-6

Witt-Eickschen, G., & O'Neill, H. S. C. (2005). The effect of temperature on the equilibrium distribution of trace elements between clinopyroxene, orthopyroxene, olivine and spinel in upper mantle peridotite. *Chemical Geology*, *221*(1–2), 65–101. https://doi.org/10.1016/j.chemgeo.2005.04.005

Woelki, D., Regelous, M., Haase, K. M., & Beier, C. (2019). Geochemical mapping of a paleo-subduction zone beneath the Troodos Ophiolite. *Chemical Geology*, *523*, 1–8. https://doi.org/10.1016/j.chemgeo.2019.05.041

Woelki, D., Regelous, M., Haase, K. M., Romer, R. H. W., & Beier, C. (2018). Petrogenesis of boninitic lavas from the Troodos ophiolite, and comparison with Izu–Bonin–mariana fore-arc crust. *Earth and Planetary Science Letters*, *498*, 203–214. https://doi.org/10.1016/j.epsl.2018.06.041

Woodhead, J. D., Eggins, S. M., & Johnson, R. W. (1998). Magma Genesis in the New Britain Island Arc. *Further Insights into Melting and Mass Transfer Processes*, *39*(9), 28.

Workman, R. K., & Hart, S. R. (2005). Major and trace element composition of the depleted MORB mantle (DMM). *Earth and Planetary Science Letters*, *231*(1–2), 53–72. https://doi.org/10.1016/j.epsl.2004.12.005

Xiong, X. L., Adam, J., & Green, T. H. (2005). Rutile stability and rutile/melt HFSE partitioning during partial melting of hydrous basalt: Implications for TTG Genesis. *Chemical Geology*, *218*(3–4), 339–359. https://doi.org/10.1016/j.chemgeo.2005.01.014

Yamaoka, K., Matsukura, S., Ishikawa, T., & Kawahata, H. (2015). Boron isotope systematics of a fossil hydrothermal system from the Troodos ophiolite, Cyprus: Water–rock interactions in the oceanic crust and subseafloor ore deposits. *Chemical Geology*, *396*, 61–73. https://doi.org/10.1016/j.chemgeo.2014.12.023

Zhang, C., Holtz, F., Koepke, J., Wolff, P. E., Ma, C., & Bédard, J. H. (2013). Constraints from experimental melting of amphibolite on the depth of formation of garnet-rich restites, and implications for models of Early Archean crustal growth. *Precambrian Research*, *231*, 206–217. https://doi.org/10.1016/j.precamres.2013.03.004

References From the Supporting Information

Adam, J., & Green, T. (2006). Trace element partitioning between mica- and amphibole-bearing garnet lherzolite and hydrous basanitic melt: 1. Experimental results and the investigation of controls on partitioning behaviour. *Contributions to Mineralogy and Petrology*, *152*(1), 1–17. https://doi.org/10.1007/s00410-006-0085-4

Aigner-Torres, M., Blundy, J., Ulmer, P., & Pettke, T. (2007). *Laser Ablation ICPMS study of trace element partitioning between plagioclase and basaltic melts: An experimental approach* (Vol. 21). Contrib Mineral Petrol.

Anguelova, M., Fehr, M. A., Takazawa, E., & Schönbächler, M. (2022). Titanium isotope heterogeneity in the Earth's mantle: A case study of the Horoman peridotite massif. *Geochimica et Cosmochimica Acta*, *335*, 356–368. S0016703722003362. https://doi.org/10.1016/j.gca.2022.07.005

Bindeman, I. N., Davis, A. M., & Drake, M. J. (1998). Ion microprobe study of plagioclase-basalt partition experiments at natural concentration levels of trace elements. *Geochimica et Cosmochimica Acta*, *62*(7), 1175–1193. https://doi.org/10.1016/S0016-7037(98)00047-7

Elkins, L. J., Gaetani, G. A., & Sims, K. W. W. (2008). Partitioning of U and Th during garnet pyroxenite partial melting: Constraints on the source of alkaline ocean island basalts. *Earth and Planetary Science Letters*, *17*(1–2), 270–286. https://doi.org/10.1016/j.epsl.2007.10.034

Fonseca, R. O. C., Kirchenbaur, M., Ballhaus, C., Münker, C., Zirner, A., Gerdes, A., et al. (2017). Fingerprinting fluid sources in Troodos ophiolite complex orbicular glasses using high spatial resolution isotope and trace element geochemistry. *Geochimica et Cosmochimica Acta*, *200*, 145–166. https://doi.org/10.1016/j.gca.2016.12.012

Green, T. H., Blundy, J. D., Adam, J., & Yaxley, G. M. (2000). SIMS determination of trace element partition coefficients between garnet, clinopyroxene and hydrous basaltic liquids at 2–7.5 GPa and 1080–1200°C. *Lithos*, *53*(3–4), 165–187. https://doi.org/10.1016/S0024-4937(00)00023-2

Hermann, J., & Rubatto, D. (2009). Accessory phase control on the trace element signature of sediment melts in subduction zones. *Chemical Geology*, *265*(3–4), 512–526. https://doi.org/10.1016/j.chemgeo.2009.05.018

Hoare, L., Klaver, M., Muir, D. D., Klemme, S., Barling, J., Parkinson, I. J., et al. (2022). Empirical and experimental constraints on Fe-Ti oxide-melt titanium isotope fractionation factors. *Geochimica et Cosmochimica Acta*, *326*, 253–272. S001670372200076X. https://doi.org/10.1016/j.gca.2022.02.011

Kirchenbaur, M., & Münker, C. (2015). The behaviour of the extended HFSE group (Nb, Ta, Zr, Hf, W, Mo) during the petrogenesis of mafic K-rich lavas: The Eastern Mediterranean case. *Geochimica et Cosmochimica Acta*, *165*, 178–199. https://doi.org/10.1016/j.gca.2015.05.030

Klaver, M., Djuly, T., de Graaf, S., Sakes, A., Wijbrans, J., Davies, G., & Vroon, P. (2015). Temporal and spatial variations in provenance of Eastern Mediterranean Sea sediments: Implications for Aegean and Aeolian arc volcanism. *Geochimica et Cosmochimica Acta*, *153*, 149–168. https://doi.org/10.1016/j.gca.2015.01.007

Klemme, S., Blundy, J. D., & Wood, B. J. (2002). Experimental constraints on major and trace element partitioning during partial melting of eclogite. *Geochimica et Cosmochimica Acta*, *66*(17), 3109–3123. https://doi.org/10.1016/S0016-7037(02)00859-1

Klemme, S., Günther, D., Hametner, K., Prowatke, S., & Zack, T. (2006). The partitioning of trace elements between ilmenite, ulvospinel, armalcolite and silicate melts with implications for the early differentiation of the moon. *Chemical Geology*, *234*(3–4), 251–263. https://doi.org/10.1016/j.chemgeo.2006.05.005

Klemme, S., Prowatke, S., Hametner, K., & Günther, D. (2005). Partitioning of trace elements between rutile and silicate melts: Implications for subduction zones. *Geochimica et Cosmochimica Acta*, *69*(9), 2361–2371. https://doi.org/10.1016/j.gca.2004.11.015

König, S., Münker, C., Hohl, S. V., Paulick, H., Barth, A. R., Lagos, M., et al. (2011). The Earth's tungsten budget during mantle melting and crust formation. *Geochimica et Cosmochimica Acta*, *75*(8), 2119–2136. https://doi.org/10.1016/j.gca.2011.01.031

König, S., Münker, C., Schuth, S., & Garbe-Schönberg, D. (2008). Mobility of tungsten in subduction zones. *Earth and Planetary Science Letters*, *274*(1–2), 82–92. https://doi.org/10.1016/j.epsl.2008.07.002

König, S., Münker, C., Schuth, S., Luguet, A., Hoffmann, J. E., & Kuduon, J. (2010). Boninites as windows into trace element mobility in subduction zones. *Geochimica et Cosmochimica Acta*, *74*(2), 684–704. https://doi.org/10.1016/j.gca.2009.10.011

Kurzweil, F., Wille, M., Gantert, N., Beukes, N. J., & Schoenberg, R. (2016). Manganese oxide shuttling in pre-GOE oceans—Evidence from molybdenum and iron isotopes. *Earth and Planetary Science Letters*, *452*, 69–78. https://doi.org/10.1016/j.epsl.2016.07.013

Mandl, M. B. (2019). *Titanium isotope fractionation on the Earth and Moon: Constraints on magmatic processes and Moon formation [Application/pdf]*. ETH Zurich. https://doi.org/10.3929/ETHZ-B-000351171

Schuth, S., Münker, C., König, S., Qopoto, C., Basi, S., Garbe-Schönberg, D., & Ballhaus, C. (2009). Petrogenesis of lavas along the Solomon Island Arc, SW Pacific: Coupling of compositional variations and subduction zone geometry. *Journal of Petrology*, *50*(5), 781–811. https://doi.org/10.1093/petrology/egp019

Sievwright, R. H., Wilkinson, J. J., O'Neill, H. S. C., & Berry, A. J. (2017). Thermodynamic controls on element partitioning between titanomagnetite and andesitic–dacitic silicate melts. *Contributions to Mineralogy and Petrology*, *172*(8), 62. https://doi.org/10.1007/s00410-017-1385-6

Storck, J.-C., Greber, N. D., Duarte, J. F. V., Lanari, P., Tiepolo, M., & Pettke, T. (2023). Molybdenum and titanium isotopic signatures of arc-derived cumulates. *Chemical Geology*, *617*, 121260. https://doi.org/10.1016/j.chemgeo.2022.121260

Tiepolo, M., Oberti, R., Zanetti, A., Vannucci, R., & Foley, S. F. (2007). Trace-Element partitioning between amphibole and silicate melt. *Reviews in Mineralogy and Geochemistry*, *67*(1), 417–452. https://doi.org/10.2138/rmg.2007.67.11

Zack, T., & Brumm, R. (1998). Ilmenite/liquid partition coefficients of 26 trace elements determined through ilmenite/clinopyroxene partitioning in garnet pyroxenites. In *International kimberlite conference extended abstracts: 1998*. University of Alberta. https://doi.org/10.29173/ikc2955

Zhang, C., Holtz, F., Koepke, J., Wolff, P. E., Ma, C., & Bédard, J. H. (2013). Constraints from experimental melting of amphibolite on the depth of formation of garnet-rich restites, and implications for models of Early Archean crustal growth. *Precambrian Research*, *231*, 206–217. https://doi.org/10.1016/j.precamres.2013.03.004